Inflammasome activation and pulmonary viral loads define two distinct clinical outcomes in COVID-19.

Keyla S.G. de Sá[1], Luana A. Amaral[1], Camila C.S. Caetano[1], Amanda Becerra[1], Sabrina S. Batah[2], Isadora M. de Oliveira[1], Letícia S. Lopes[1], Leticia Almeida[1], Samuel Oliveira[1], Danilo Tadao Wada[3], Marcel Koenigkam-Santos[3], Ronaldo B. Martins[1], Roberta R. C. Rosales[1], Eurico Arruda[1], Alexandre T Fabro[2], Dario S. Zamboni[1*].

[1]Departamento de Biologia Celular e Molecular e Bioagentes Patogênicos, Faculdade de Medicina de Ribeirão Preto, Universidade de São Paulo, Ribeirão Preto, SP, 14049-900, Brazil.

[2]Departamento de Patologia e Medicina Legal, Faculdade de Medicina de Ribeirão Preto, Universidade de São Paulo, Ribeirão Preto, SP, 14049-900, Brazil.

[3]Departamento de Imagens Médicas, Hematologia e Oncologia, Faculdade de Medicina de Ribeirão Preto, Universidade de São Paulo, Ribeirão Preto, SP, 14049-900, Brazil.

*Correspondence:

Email: dszamboni@fmrp.usp.br

Abstract

Inflammasome activation is associated with disease severity in patients who are infected with SARS-CoV-2 and influenza viruses, but the specific cell types involved in inflammasome activation, as well as the balance of inflammasome activation versus viral replication in COVID-19 exacerbation and the induction of patient death, are unknown. In this study, we assessed lung autopsies of 47 COVID-19 and 12 influenza fatal cases and examined the inflammatory profiles and inflammasome activation; additionally, we correlated these factors with clinical and histopathological patient conditions. We observed an overall stronger inflammasome activation in lethal cases of SARS-CoV-2 compared to influenza and found a different profile of inflammasome-activating cells during these diseases. In COVID-19 patients, inflammasome activation is mostly mediated by macrophages and endothelial cells, whereas in influenza, type I and type II pneumocytes contribute more significantly. An analysis of gene expression allowed for the classification of COVID-19 patients into two different clusters. Cluster 1 (n=16 patients) died with higher viral loads and exhibited a reduced inflammatory profile than Cluster 2 (n=31 patients). Illness time, mechanical ventilation time, pulmonary fibrosis, respiratory functions, histopathological status, thrombosis, and inflammasome activation significantly differed between the two clusters. Our data demonstrated two distinct profiles in lethal cases of COVID-19, thus indicating that the balance of viral replication and inflammasome-mediated pulmonary inflammation may lead to different clinical conditions, yet both lead to patient death. An understanding of this process is critical for decisions between immune-mediated or antiviral-mediated therapies for the treatment of critical cases of COVID-19.

Introduction

Influenza viruses and epidemic coranaviruses are the most frequent viral agents of acute respiratory distress syndrome (ARDS). Between 2019 and 2021, there were 35,000,000 symptomatic cases of influenza with approximately 20,000 deaths in the United States [1] and more than 255,000,000 confirmed cases and 5,127,000 deaths caused by the severe acute respiratory syndrome coronavirus 2 (SARS-CoV-2) worldwide [2]. Severe ARDS is characterized by major pulmonary involvement, respiratory distress, systemic thrombosis, and death [3-5].

The activation of the NLRP3 inflammasome has been described both in influenza [6-10] and SARS-CoV-2 infections [11-16], and this process contributes to excessive inflammation and poor clinical outcome. The recruitment of immune cells to the lungs of infected individuals culminates in the excessive release of cytokines that cause structural damage to the lungs [17, 18]. Moreover, the major reported lung pathologies of severe COVID-19 include diffuse alveolar damage (DAD), acute fibrinoid organizing pneumonia (AFOP), and chronic interstitial pneumonia [3-5, 19]. NLRP3 inflammasome activation also occurs in the lung parenchyma of these patients [16, 20]. For influenza, the major reported lung pathologies include diffuse alveolar damage in addition to necrotizing bronchitis, bronchiolitis, and fibrosis [21]. However, it is still unknown as to how the activation of this immune complex is related to the exacerbated inflammatory process in human lung parenchyma cells during viral infections such as influenza and SARS-CoV-2.

In the present study, postmortem lung tissue samples from 47 fatal COVID-19 patients and 12 fatal influenza patients were examined for inflammasome activation and gene expression; in addition, these factors were correlated with the clinical conditions of the patients to understand the molecular mechanisms underlying the pathological processes that lead to the death of these patients. We demonstrated the presence of robust inflammasome activation in the lungs of patients infected with SARS-CoV-2 and influenza virus and defined the specific cell types that contribute to inflammasome activation in response to these viruses. An analysis of

gene expression in pulmonary tissues allowed for the classification of COVID-19 patients into two different clusters (one cluster with patients who died with higher viral loads and reduced inflammatory profiles, which opposes the data from the other cluster). Our data indicated that inflammasome activation by different cell types contributes to the pathology of influenza and COVID-19, thus indicating that a distinct balance in viral replication and inflammation may culminate with patient death in COVID-19.

Materials and Methods

Samples

Minimally invasive autopsy was performed on 47 patients diagnosed with SARS-CoV-2 at the Hospital das Clínicas da Faculdade de Medicina de Ribeirão Preto da Universidade de São Paulo, Brazil (Ribeirão Preto, SP, Brazil) from April to July, 2020, by Serviço de Patologia (SERPAT). Minimally invasive autopsy was done at bedside through post-mort surgical lung biopsy by a matching 14-gauge cutting needle (Magnum Needles, Bard) and a biopsy gun (Magnum, Bard). Moreover, a 3 cm incision on the more affected side of the chest between the fourth and fifth ribs were also used to provide extra lung tissue. All tissue samples were embedded in paraffin and fixed in formalin (Formalin-Fixed Paraffin- Embedded, FFPE). Lung tissue from autopsies of patients diagnosed with Influenza (n=12) of patients who died between the years 2012 to 2020 and biopsy of Lung Adenocarcinoma patients (n=5) were obtained from SERPAT. The project was approved by the Research Ethics Committee of FMRP/USP under protocol nº 4,089 .567.

Immunohistochemistry (IHC)

Tissue section in paraffin blocks were tested by immunohistochemistry using antibodies for the detection of NLRP3 (clone D2P5E; 1:3,000; Cell Signaling), ASC (1:2,000; Adipogen AL177), SFTPC (1:200, ThermoFisher PA5-71680), CD68 (1:200, Dako M0814), CD34 (1:500, Zeta Z2063ML), PDPN (1:200, ThermoFisher 14-9381-82), THY-1 (1:300, Sigma SAB4200497), Vimentin (1:200, Sigma V2258), Anti-cleaved N-terminal GSDMD (1:200, Abcam ab215203), Caspase-1 (1:200,

120 Abcam ab207802), IL-1β (1:200, Abcam ab2105) for the *in situ* detection of these
121 inflammasome proteins. The Sequential Immunoperoxidase Labeling and Erasing
122 (SIMPLE) technique was used to evaluate all markers in the same tissue, as
123 previously published [22]. Briefly, after incubation with primary antibody (overnight at
124 4ºC), slides were incubated with immune peroxidase polymer anti-mouse
125 visualization system (SPD-125, Spring Bioscience, 345 Biogen) and with
126 chromogen-substrate AEC peroxidase system kit (SK-4200, 346 Vector
127 Laboratories, Burlingame, CA). After high resolution scanning by a VS120 Olympus
128 microscope, the coverslips were removed in PBS and the slides were dehydrated in
129 an ethanol gradient to 95% ethanol. The slides were incubated in a series of ethanol
130 to erase the AEC marking. Afterwards the slides were rehydrated and the
131 antibodies were removed with an incubation for 2 min in a solution of 0.15 mM 351
132 KMnO4/0.01 M H_2SO_4, followed immediately by a wash in distilled water. Tissues
133 were then remarked.

134

135 ***Immunofluorescence***

136 The slides were incubated with the primary antibodies, rabbit anti-human NLRP3
137 mAb (clone D2P5E; 1:300; Cell Signaling), rabbit anti-human ASC polyclonal
138 antibody (1:200; Adipogen AL177), SFTPC (1:200, ThermoFisher PA5-71680),
139 CD64 (1:200, Biolegend 139304), CD34 (1:500, Zeta Z2063ML), PDPN (1:200,
140 ThermoFisher 14-9381-82), overnight at 4ºC and with the secondary antibodies
141 Goat anti-mouse Alexa fluor-647 (Invitrogen) or Goat anti-rabbit Alexa fluor-594
142 (Invitrogen). Images were acquired by the Axio Observer system combined with the
143 LSM 780 confocal device microscope at 63x magnification (Carl Zeiss).

144

145 ***Histological Evaluation***

146 Paraffin-embedded lung tissues sections (3 µm) were stained by standard
147 hematoxylin and eosin (H&E). Morphological lung injury patterns were evaluated by
148 specialized pulmonary pathologists (ATF) blinded to clinical history. They were
149 classified as absent or present with its extent of lung injury area by 5% cut-offs in
150 Fibrosis, Organizing Pneumonia (OP), Acute Fibrinous and Organizing Pneumonia
151 (AFOP), Diffuse Alveolar Damage (DAD), Cellular Pneumonitis, Thrombus
152 Formation.

153

154 ***RNA extraction***

155 RNA from influenza samples and respective controls was extracted from Paraffin-
156 embedded tissue samples. Samples were cut into 3 sections of 10 µm, and placed
157 in RNase-free, 2.0-ml Eppendorf tubes. Sections were deparaffinized by incubation
158 in 0.8 ml of xylene at 37°C for 5 minutes. The samples were then centrifuged, the
159 supernatant was removed, and fresh xylene was added for a second incubation.
160 After deparaffinization and centrifugation, sections were washed with 0.8 ml
161 ethanol, air-dried for several minutes, and resuspended in 25 µl of 20 mg/ml
162 Proteinase K (Gibco BRL, Gaithersburg, MD) plus 720 µl of a digestion buffer with
163 the following final concentrations: 20mM TRIS-HCl pH8, 10mM EDTA pH8, 1% of
164 SDS. Samples were vortexed and incubated overnight at 55°C at 400 rpm. A
165 second 25 µl aliquot of 20 mg/ml Proteinase K was then added, followed by
166 vortexing and incubation for 2h at 55°C. RNA was obtained by extraction with 1 mL
167 of Trizol reagent and purification was performed according to the manufacturer's
168 instructions. Total RNA from fresh lung tissue of SARS-CoV-2 patients and
169 respective controls was obtained using Trizol reagent and purification was
170 performed according to the manufacturer's instructions. The RNA was quantified by
171 spectrophotometry in a NanoDrop 2000c spectrophotometer. The concentration
172 was adjusted to 1 µg/µL, and the RNA was stored at −70 ◦C until reverse
173 transcription.

174

175 ***Real-Time Polymerase Chain Reaction for inflammatory genes***
176 For inflammatory genes qPCR the total RNA was transcribed into complementary
177 DNA (cDNA) using a High-Capacity cDNA Reverse Transcription kit (without an
178 inhibitor) according to the protocol provided by the manufacturer (Thermo Fisher,
179 Carlsbad, CA, USA). The reaction was prepared in a final volume of 20.0 µL
180 containing 4.2 µL of H_2O, 2.0 µL of buffer, 2.0 µL of random primers, 0.8 µL of
181 dNTP Mix (100 mM), 1.0 µL of reverse transcriptase (RT) enzyme and 1 µL of RNA
182 (1 ug/µL). The solution was then placed into a thermocycler with the following
183 program: 25 ◦C for 10 min, 37 ◦C for 120 min and 85 ◦C for 5 min. The real-time
184 PCR was performed in 96-well plates using Sybr Green reagents (Applied
185 Biosystems, Waltham, MA, USA) and a Quant studio real-time PCR system
186 (Applied Biosystems, Foster City, CA, USA). The real time-RT-PCR was carried out
187 in a total volume of 20 µl on a 96-well MicroAmp Fast Optical plate (Applied
188 Biosystems). Each well contained 10 µl SYBR Green qPCR Master Mix
189 (Thermofisher), 1 µl of each primer (**Supplementary Table 1**), 2 µl cDNA (20 ng)
190 and 7 µl RNase free water using the following protocol: initial denaturation at 95°C

191 for 10 min, 40 cycles of denaturation at 95°C for 15 s followed by
192 annealing/extension at 60°C for 60 s. Each PCR was followed by a dissociation
193 curve analysis between 60-95°C. The Ct values were analyzed by the comparative
194 Ct (ΔΔCt) method and normalized to the endogenous control GAPDH. Fold
195 difference was calculated as $2^{-\Delta\Delta Ct}$

196

197 ***Real-Time Polymerase Chain Reaction for Viral RNA***

198 Detection and quantification of SARS-CoV-2 genes was performed with primer-
199 probe sets for 2019-nCoV_N2 and gene E, according to US Centers for Disease
200 Control and Prevention [23] and Charité group protocols [24]. The genes evaluated (N2,
201 E, and RNase-P housekeeping gene) were tested by one-step real-time RT-PCR
202 using total nucleic acids extracted with TRIzol (Invitrogen). All real-time PCR assays
203 were done on a Quant studio real-time PCR system (Applied Biosystems, Foster
204 City, CA, USA). A total of 70 ng of RNA was used for genome amplification, adding
205 specific primers (20 μM), and probe (5 μM), and with TaqPath 1-Step quantitative
206 RT-PCR Master Mix (Applied Biosystems), with the following parameters: 25°C for 2
207 min, 50°C for 15 min, and 95°C for 2 min, followed by 45 cycles of 94°C for 5 s and
208 60°C for 30 s. Primers used were the following: N2 forward: 5′-
209 TTACAAACATTGGCCGCAAA-3′, N2 reverse: 5′-GCGCGACATTCCGAAGAA-3′;
210 N2 probe: 5′-FAM-ACAATTTGCCCCCAGCGCTTCAG-BHQ1-3′ [23]; E forward: 5′-
211 ACAGGTACGTTAATAGTTAATAGCGT-3′, E reverse: 5′-
212 ATATTGCAGCAGTACGCACACA-3′; E probe: 5′-AM-
213 ACACTAGCCATCCTTACTGCGCTTCG-BHQ-1-3′ [24]; RNase-P forward: 5′-
214 AGATTTGGACCTGCGAGCG-3′, RNase-P reverse: 5′-
215 GAGCGGCTGTCTCCACAAGT-3′; and RNase-P probe: 5′-FAM-
216 TTCTGACCTGAAGGCTCTGCGCG-BHQ-1-3′ [23]. A plasmid of N2 protein and E
217 protein was used for a standard curve construction for viral load quantification.

218

219 ***Chest computed tomography images acquisition and evaluation***

220 Chest x-radiography (CXR) and computed tomography (CT) exams were performed
221 as part of the routine clinical evaluation. Chest radiographies were performed in
222 conventional equipment, mainly in the anteroposterior incidence. CT images were
223 performed in multidetector scanners (Brilliance CT Big Bore 16 - Philips, Holland, or
224 Aquilion Prime 160 - Toshiba, Japan), using similar protocols for the acquisition of
225 high-resolution images of the lungs [25]. Patients were scanned in the supine position

226 without the administration of intravenous contrast media. Typical acquisition
227 parameters were: 120 kVp tube voltage, 100–140 ref mAs [26], 0.3–0.7 s gantry
228 rotation time, reconstruction matrix size of 512×512, slice thickness, and increment
229 of 1.0 mm, using standard (soft) and hard kernel filters. Imaging exams were
230 independently evaluated by two thoracic radiologists (MKS and DTW), blinded to
231 clinical data, laboratory, and pathology results as described [26]. Divergences were
232 solved by consensus. All CXRs available were classified for the presence and grade
233 of viral pneumonia [27]. Pulmonary disease evolution on imaging was evaluated
234 considering all exams from the initial to the last image before death. Tomographic
235 images were evaluated similarly to CXR images.

236

237 ***Statistical Analysis***

238 For puncta quantification, all histological sections were viewed on a 63x objective
239 for digitalizing random images using the LSM 780 system in the Axio Observer
240 microscope, covering an area of about ~1.7 mm^2 of lung parenchyma analyzed per
241 case. Manual counting of puncta and cells was blinded and performed using the
242 acquired images. Morphometric analyzes were performed as described [28]. The
243 quantification of expression by immunohistochemistry was performed by calculating
244 the percentage of marked area, the scanned images were opened in the ImageJ
245 software, using the IHQ Toolbox plugin, which consists of a semi-automatic color
246 selection tool that selects the pixels positive for immunohistochemical marking,
247 differentiating them from background and H&E marking, after selecting the positive
248 pixels, the images were transformed into 8-bits and the area occupied by these
249 tones was calculated. The distribution of the gene expression and biochemical
250 marker and puncta count data was evaluated using the Shapiro–Wilk test; the data
251 were analyzed using non-parametric Kruskal-Wallis, Mann-Whitney test and
252 Spearman correlation. Data were presented in graphs with mean and standard
253 deviation. Statistical analyzes were performed using the GraphPad PRISM 5.0
254 program, with $p<0.05$ being considered statistically significant. Heatmaps were
255 constructed using the heatmap.2 function in the R program (Project for Statistical
256 Computing, version 3.4.1).

257

Results

Lethal cases of COVID-19 develop severe acute respiratory distress syndrome (ARDS) and higher inflammasome activation in the lung parenchyma than influenza patients

We evaluated inflammasome activation in the lung parenchyma of 47 patients who died from SARS-CoV-2 infection from April to July 2020. These patients were infected with the ancestral strain of SARS-CoV-2 before the development of the COVID-19 variants of concern and before the use of vaccinations. We also evaluated 12 patients who died from influenza before the COVID-19 pandemic. As a noninfected control, we evaluated inflammasome activation in biopsies of the benign area of the lungs from patients who died due to lung adenocarcinoma. The data in **Table 1** show the demographic and clinical characteristics of the influenza and COVID-19 patients. COVID-19 patients had a higher mean age (67.97 years) than influenza patients (41.5 years). Most of the influenza patients were infected with subtype A H1N1 (41.66%) but also with subtypes A H3N2 (16.66%) and B (16.66%). In addition, according to the data observed in the COVID-19 cases that occurred in 2020 (patients infected with the ancestral Wuhan strain of SARS-CoV-2), we found that COVID-19 patients had a higher frequency of comorbidities, such as hypertension, in addition to having (on average) grade 1 obesity (BMI: 31.10). Furthermore, patients with influenza and COVID-19 (on average) exhibited altered values of CRP, D-dimers, LDH, creatinine, urea, AST, ALT, PT (INR), and blood glucose levels. Moreover, patients with influenza presented with a fulminant picture of ARDS and died (on average) less than 24 hours after seeking health services. In contrast, patients with COVID-19 had an average illness time of 18 days, and the vast majority (76.59%) of the patients used MV, with an average of 12.38 days of use of mechanical ventilation. Moreover, COVID-19 patients had a more severe respiratory condition than influenza patients, with a considerably altered PaO_2 and PaO_2/FiO_2 characterizing a moderate to severe ARDS condition (**Table 1**). Consistent with the respiratory statuses of the patients, the histopathological analyses of COVID-19 patients demonstrated a higher fibrotic phase of DAD, OP, and pneumonitis than those of influenza patients (**Figure 1A-C**). To analyze histological features of patients' lungs, we measured the lung parenchyma area in the histological sections. In support of the data described above, we observed that

295 patients who died from SARS-CoV-2 and influenza had a much larger area of lung
296 parenchyma than adenocarcinoma patients, but no difference was found in
297 influenza versus COVID-19, thus supporting the idea that both viral infections
298 trigger robust inflammatory infiltration to the lung in severe cases of the disease
299 (**Figure 1D-G**). These data are in agreement with histopathological findings
300 showing an intense inflammatory process in patients who died from SARS-CoV-2
301 and influenza [3, 29].
302
303 To assess inflammasome activation in the lungs of COVID-19 and influenza
304 patients, the lung parenchyma area and cell count were scanned in histological
305 sections by using 2-photon microscopy. The parenchyma area was calculated by
306 using ImageJ software, and inflammasome activation was microscopically scored
307 by the presence of characteristic NLRP3 or ASC puncta/specks [30]. The parenchyma
308 area was used to normalize all of the counts between the patients. Inflammasome
309 activation was quantified by counting ASC and NLRP3 puncta in the lung tissue of
310 these patients. We observed that patients with SARS-CoV-2 infection had more
311 ASC and NLRP3 puncta than patients with influenza and controls with lung
312 adenocarcinoma (**Figure 1H, J**). Representative images of ASC and NLRP3 puncta
313 in the patients' lungs are shown (**Figures 1I, K)**. We observed ASC colocalization in
314 nearly all of the scored NLRP3 puncta, thus confirming that these puncta structures
315 that were abundantly found in the patients' lungs are indeed the NLRP3/ASC
316 inflammasome (**Figure 1L, M**). Collectively, these data indicate that COVID-19
317 patients have higher inflammasome activation than influenza patients and that these
318 patients evolved to a fibrotic phase of DAD, OP, and pneumonitis.
319

320

321

322 ***The cellular profile of inflammasome activation differs in lethal cases of***
323 ***COVID-19 and influenza***

324

325 To comprehensively investigate the cell types operating during influenza and SARS-
326 CoV-2 infection, we analyzed the presence of macrophages (CD64$^+$), endothelial
327 cells (CD34$^+$), type 1 pneumocytes (PDPN$^+$, Podoplanin$^+$), and type 2 pneumocytes
328 (SFTPC$^+$) in the lungs of patients who died from SARS-CoV-2 infection and
329 influenza. We found that total counts of macrophages and endothelial cells were not
330 different between COVID-19 and influenza patients and were also similar to those
331 observed in the benign area of lung adenocarcinoma (**Figure 2A, 2B**). However, we
332 observed that patients who died from influenza had fewer type 1 pneumocytes and
333 type 2 pneumocytes (**Figure 2C, 2D**), which is consistent with data indicating that
334 the influenza virus preferentially infects type 1 and type 2 pneumocytes than
335 macrophages and promotes the death of these cells due to the viral replication
336 process [31]. Next, we evaluated the participation of specific cells in inflammasome
337 activation by scoring ASC and NLRP3 puncta in macrophages (CD64$^+$), endothelial
338 cells (CD34$^+$), type 1 pneumocytes (PDPN$^+$), and type 2 pneumocytes (SFTPC$^+$).
339 We observed that in the lungs of COVID-19 patients, both ASC and NLRP3 puncta
340 were more frequently found in macrophages (**Figure 2E, I**) and endothelial cells
341 (**Figure 2F, J**) than in influenza patients. In contrast, in the assessment of type 1
342 and type 2 pneumocytes, we found that ASC and NLRP3 puncta were more
343 frequently observed in the lungs of influenza patients than in COVID-19 patients
344 (**Figure 2G, H, K, L**). Representative images of ASC and NLRP3 puncta in
345 macrophages, endothelial cells, and type 1 and type 2 pneumocytes are shown in
346 **Figure 2M-T**. Together, these data demonstrate for the first time that distinct
347 pulmonary cell types can trigger inflammasome activation in COVID-19 and
348 influenza; additionally, the data indicate a main contribution of macrophages and
349 endothelial cells to inflammasome activation during SARS-CoV-2 and type I and II
350 pneumocytes to inflammasome activation during influenza. The magnitude of
351 inflammasome activation and the different cellular profiles of inflammasome
352 activation between COVID-19 and influenza may contribute to explaining the overall
353 increased inflammasome activation found in COVID-19 compared to influenza.

354

355 Subsequently, we performed immunohistochemistry analyses of the lung
356 parenchyma to assess the expression of inflammasome components and observed
357 variable expression of NLRP3, ASC, cleaved GSDMD, IL-1β, and caspase-1 in
358 COVID-19 and influenza (**Supplementary Fig. 1A-E**). To assess which lung
359 parenchyma cells expressed these inflammasome components, we evaluated the
360 expression of ASC, NLRP3, caspase-1, cleaved GSDMD, and IL-1β on endothelial
361 cells ($CD34^+$), macrophages ($CD68^+$), and type 2 pneumocytes ($SFTPC^+$) via
362 immunohistochemistry (**Supplementary Fig. 1F-H**). We also stained these tissues
363 with anti-Spike of SARS-CoV-2 and found that virus-associated endothelial cells,
364 macrophages, and type 2 pneumocytes expressed ASC, NLRP3, Caspase-1, and
365 IL-1β (**Supplementary Fig. 1F-H**).

366

367 ***Disease progression in lethal cases of COVID-19 occurs with decreasing viral***
368 ***load and increasing inflammasome activation over time in the lung***
369 ***parenchyma***

370

371 To assess whether inflammasome activation was associated with specific patient
372 clinical conditions, we performed Pearson's correlations in COVID-19 patients. Even
373 though all of these patients died, we observed a strong negative correlation
374 between viral load and the extent of the disease (**Figure 3A, B**). In addition, we
375 observed a positive correlation between the amount of NLRP3 and ASC puncta with
376 the time of disease (**Figure 3C, D**), thus suggesting that, in general, whereas the
377 viral load is reduced, inflammasome activation increases during hospitalization in
378 these lethal cases of COVID-19. We also observed significant negative correlations
379 between NLRP3 puncta and PaO_2/FiO_2 (**Figure 3E**), thus suggesting that
380 inflammasome activation is related to an overall worsening pulmonary function. We
381 detected no statistically significant correlations between NLRP3 or ASC puncta and
382 viral load in the tissues (**Supplementary Fig. 2**).

383

384 **Inflammasome activation and pulmonary viral loads defines two distinct**
385 **clinical outcomes in lethal cases of COVID-19.**

386

387 The imbalance of inflammatory and anti-inflammatory processes leads to an
388 excessive release of cytokines into the systemic circulation with potentially
389 deleterious consequences, including systemic inflammatory response syndrome

390 (SIRS), circulatory shock, multiorgan dysfunction syndrome (MODS), and death [32].
391 Several studies have reported the association of influenza [33-37] and SARS-CoV-2 [38-
392 40] with hyperinflammatory syndrome related to disease severity, and inflammasome
393 activation may be associated with Cytokine Release Syndrome (CRS) [41-43]. Thus, to
394 correlate inflammasome activation with the hyperinflammatory profile observed in
395 lethal cases of COVID-19, we analyzed the expression of genes related to the
396 inflammatory process and inflammasome activation. We evaluated gene expression
397 in the lungs of COVID-19 patients and observed that several inflammatory cytokine
398 genes have a positive correlation with the genes involved in inflammasome
399 activation (**Supplementary Fig. 3A**). We did not observe a significant difference in
400 the expression of these genes when we compared COVID-19 patients with lung
401 adenocarcinoma patients (**Supplementary Fig. 3B-U**), possibly due to the large
402 dispersion of data observed in COVID-19 patients. Due to this dispersion and high
403 variation in gene expression detected in COVID-19 patients, we performed an
404 unsupervised heatmap constructed with data from relative gene expression and
405 revealed the formation of two clusters in COVID-19 patients (**Figure 4A**). Cluster 1
406 was characterized by a higher viral load and lower expression of inflammasome and
407 inflammatory genes. In contrast to Cluster 1, Cluster 2 was comprised of patients
408 who died with a lower viral load and increased expression of inflammasome and
409 inflammatory genes (**Figure 4A**). To gain insights into key differences between
410 these two clusters, we analyzed PaO_2/FiO_2 and A-a O_2 gradient kinetics in these
411 patients. We observed that patients in Cluster 2, who had overall increased
412 inflammation, had worsening pulmonary function compared to those in Cluster 1
413 (**Figure 4B, C**). By contrast, patients of Cluster 1 had disseminated intravascular
414 coagulation (**Table 2**), according to the parameters recommended by the
415 International Society of Thrombosis and Hemostasis (ISTH) [44]. Basic demographic
416 information stratified by cluster is provided in **Table 2**. Strikingly, patients who
417 belonged to Cluster 2 had a longer illness time (**Figure 4D**), worse pulmonary
418 function (as indicated by the PaO_2/FiO_2 and A-a O_2 gradients) (**Figure 4E, F**), a
419 larger area of pulmonary fibrosis (**Figure 4G**), and greater activation of the NLRP3
420 inflammasome, as measured by puncta formation (**Figure 4H**). Representative
421 images of the lung parenchyma of three representative patients in Cluster 1 and
422 three representative patients in Cluster 2 are shown in **Figure 4I-J**. In addition, we
423 confirmed that patients belonging to Cluster 2 had an overall lower viral load than
424 patients from Cluster 1 (**Supplementary Fig. 4A, B**). Next, we assessed
425 radiological analyses of 16 patients from Cluster 1 and 31 patients from Cluster 2 by
426 comparing the first and last chest X-ray images (CXR) and observed overall

427 worsening pulmonary conditions in patients from Cluster 2 (**Supplementary Fig.**
428 **5A**). Representative images of CXR of 2 patients from each cluster are shown in
429 **Supplementary Fig. 5B, C**. **Table 3** summarizes the general imaging evaluation
430 findings for the patients in Cluster 1 and Cluster 2. Taken together, our data suggest
431 the existence of two distinct groups of patients who succumbed to COVID-19, one
432 group, with lower viral loads, higher inflammation, increased fibrosis and worse
433 pulmonary conditions than the other group.

434

435

Discussion

Although SARS-CoV-2 and influenza share many similarities, including the transmission, replication, and induction of similar clinical outcomes in humans, COVID-19 can be significantly more severe in nonvaccinated individuals [45-48]. The mechanisms underlying these differences are unknown, and the revelation that exacerbated inflammasome activation mediates COVID-19 pathology [13, 14, 16] has led to comparisons of inflammasome activation in COVID-19 patients with other pulmonary viral diseases. Therefore, we assessed pulmonary samples of lethal cases of COVID-19 and influenza and determined the cellular profile of inflammasome activation in patients' lungs. Lethal cases of COVID-19 exhibited an overall greater inflammasome activation, in addition to having a different cellular activation profile, compared to lethal cases of influenza. This different profile of inflammasome activation can be partially explained by the tropism of each virus. Whereas the influenza virus almost exclusively infects pneumocytes, with minor involvement of macrophages, SARS-CoV-2 associates with a broad range of immune cells, including macrophages and structural cells, such as type 2 pneumocytes, club-like cells, goblet cells, and endothelial cells [31, 49-52]. Thus, it is possible that the large number of cell types that can be infected by SARS-CoV-2 may be a determining factor for the increased activation of the inflammasome observed in fatal cases of COVID-19 compared to influenza viruses. In addition, reduced inflammasome activation in influenza patients can be partially explained by the NS1 protein of the influenza A virus, which inhibits the NLRP3 inflammasome by suppressing ASC ubiquitination [53]. Moreover, whereas a protective role of the inflammasome has never been reported for COVID-19, these platforms account for protective antiviral immunity against influenza infection [54, 55]. Therefore, it is possible that influenza patients with higher inflammasome activation undergo a resolution of infection; as a result, these patients do not seek hospitalizations, as often occurs with COVID-19 patients.

Macrophages are possibly the most effective cell types that trigger inflammasome activation [56]; according to this information, our data showed that macrophages in the lungs of COVID-19 and influenza patients are effectively infected and strongly induce inflammasome activation. These data are in agreement with previously

472 published articles indicating high levels of viral RNA in lung monocytes and
473 macrophages of COVID-19 patients [57, 58], as well as pronounced inflammasome
474 activation in macrophages from COVID-19 patients [13, 14, 16]. In contrast, the
475 influenza virus, which effectively replicates in type I and type II pneumocytes,
476 promotes exacerbated inflammasome activation and the depletion of these cells in
477 the lungs of fatal cases of influenza. It is possible that the inflammasome and
478 pyroptosis of type I and II pneumocytes during influenza infection contribute to the
479 clinical symptoms and clinical outcomes of this disease. Importantly, this appears to
480 be the first report of inflammasome activation in type 1 and type 2 pneumocytes in
481 the lung, as the description of inflammasome activation in pneumocytes was
482 previously restricted to the A549 cell lineage [59-61]. Remarkably, inflammasome
483 activation in pneumocytes is more pronounced in patients infected with the
484 influenza virus. It is possible that inflammasome activation in pneumocytes is
485 favored by influenza virus tropism in these cells [31, 49].

486

487 In addition to inflammasome activation in pneumocytes, the analysis of
488 inflammasome activation in different pulmonary cell types indicates that endothelial
489 cells exposed to SARS-CoV-2 express inflammasome proteins and contain active
490 NLRP3/ASC puncta, thus demonstrating inflammasome activation. Despite reports
491 indicating that endothelial cells are not productively infected by SARS-CoV-2 [62],
492 precursors of hematopoietic and endothelial cells stimulated with SARS-CoV-2
493 spike protein increase the expression of *AIM2*, *NLRP1*, *NLRP3*, *IL1B*, and *ASC* and
494 trigger caspase-1 activation [63, 64]. In addition, inflammasome activation in
495 endothelial cells has been previously reported [65-68]. These observations are
496 consistent with our data indicating the expression of inflammasome components
497 and inflammasome activation in CD34+ cells in the lungs of COVID-19 patients.
498 Although these cells were stained positive for the SARS-CoV-2 spike protein, it is
499 unknown whether infection and viral replication are required for inflammasome
500 activation in these cells. It is possible that spike stimulation is sufficient for
501 inflammasome activation, which is a feature that would explain reports indicating
502 damage and dysfunction of these cells during COVID-19 and the characterization of
503 COVID-19 as an endothelial disease [69-74]. It is important to highlight the fact that the
504 vascular endothelium is actively involved in the regulation of inflammation and
505 thrombus formation. This is particularly important in COVID-19 because the
506 interplay between inflammasome activation in macrophages and the endothelium
507 can lead to pyroptotic macrophages releasing tissue factor (TF), which is an

508 essential initiator of coagulation cascades that are frequently observed in severe
509 cases of COVID-19 [75-77]. These data support the association of inflammasomes with
510 the coagulopathy that is observed in COVID-19.

511

512 Regardless of the cell type involved in inflammasome activation and comparisons
513 with influenza, our robust analysis of 47 COVID-19 patients allowed for the
514 classification of the patients into two groups. Cluster 2, which was composed of 31
515 patients, demonstrated remarkably high inflammasome activation and expression of
516 inflammatory genes with increased fibrosis in patients' lungs. Inflammatory
517 cytokines released upon inflammasome activation have been previously linked to
518 the development of pulmonary fibrosis [78-83]. In addition, cytokines such as IL-1β, IL-
519 18, and IL-1α have been described as triggering the activation of fibroblasts and
520 stimulating the synthesis and accumulation of type I collagen, TIMP, collagenase,
521 and PGE2 [78, 84], which may contribute to the triggering of the deleterious effects of
522 inflammasomes in patients' lungs.

523

524 Our findings showed that the viral load in the lungs of COVID-19 patients is
525 inversely proportional to the duration of the disease, as has been suggested in
526 previous studies [85, 86]. In addition, we collected data indicating that increased illness
527 time is associated with increased inflammasome activation, and a reduced viral load
528 implies a dysregulated immune response in which inflammation persists, whereas
529 the viral load declines. In this context, it is possible that inflammasome activation in
530 these patients occurs not as a result of the viral infection itself but by the presence
531 of damage-associated molecular patterns that are generated during the
532 inflammatory process. We also tested whether the mechanical ventilation used in
533 COVID-19 patients would interfere with inflammasome activation. This hypothesis is
534 supported by data indicating that mechanical ventilation-induced hyperoxia can
535 induce potassium efflux through the P_2X_7 receptor, thus leading to inflammasome
536 activation and the secretion of proinflammatory cytokines [43, 87-91]. However, when
537 we separated the COVID-19 patients into two groups according to the use or non-
538 use of mechanical ventilation, we detected no differences in histopathological
539 analyses and inflammasome activation (**Table 4**). Moreover, we confirmed that
540 patients who underwent mechanical ventilation had a longer illness time, higher
541 hypertension, less CRP and albumin, higher amounts of urea, and worsened
542 pulmonary function (according to the PaO2/FiO2 and A-an O2 gradients). Thus, our

data do not support the hypothesis that mechanical ventilation is directly associated with inflammasome activation. Nonetheless, we demonstrated (for the first time) a cellular profile of inflammasome activation in the lungs of patients who died from COVID-19 and influenza. Importantly, the identification of two distinct profiles in lethal cases of COVID-19 (which revealed the balance of viral loads versus inflammasome-mediated pulmonary inflammation) will be critical for decisions between immune-mediated or antiviral-mediated therapies for the treatment of critical cases of COVID-19.

Acknowledgments: We would like to thank Maira Nakamura, Amanda Zuin and Dr. Roberta Sales for technical support.

Funding: Fundação de Amparo à Pesquisa do Estado de Sao Paulo, FAPESP grants 2013/08216-2, 2019/11342-6 and 2020/04964-8. Conselho Nacional de Desenvolvimento Científico e Tecnológico, CNPq grant 303021/2020-9. Coordenação de Aperfeiçoamento de Pessoal de Nível Superior, CAPES grant 88887.507253/2020-00.

Competing interests: Authors declare that they have no competing interests.

References

1. Centers for Disease Control and Prevention , N.C.f.I.a.R.D.N. (2021).
2. WHO (World Health Organization, https://covid19.who.int/; 2020).
3. Batah, S.S. & Fabro, A.T. Pulmonary pathology of ARDS in COVID-19: A pathological review for clinicians. *Respir Med* **176**, 106239 (2021).
4. Bösmüller, H., Matter, M., Fend, F. & Tzankov, A. The pulmonary pathology of COVID-19. *Virchows Arch* **478**, 137–150 (2021).
5. Polak, S.B., Van Gool, I.C., Cohen, D., von der Thüsen, J.H. & van Paassen, J. A systematic review of pathological findings in COVID-19: a pathophysiological timeline and possible mechanisms of disease progression. *Mod Pathol* **33**, 2128-2138 (2020).
6. Allen, I.C. *et al.* The NLRP3 inflammasome mediates in vivo innate immunity to influenza A virus through recognition of viral RNA. *Immunity* **30**, 556-565 (2009).
7. Boal-Carvalho, I. *et al.* Influenza A viruses limit NLRP3-NEK7-complex formation and pyroptosis in human macrophages. *EMBO Rep* **21**, e50421 (2020).
8. Ichinohe, T., Pang, I.K. & Iwasaki, A. Influenza virus activates inflammasomes via its intracellular M2 ion channel. *Nat Immunol* **11**, 404-410 (2010).
9. Moriyama, M. *et al.* Influenza Virus-Induced Oxidized DNA Activates Inflammasomes. *iScience* **23**, 101270 (2020).
10. Thomas, P.G. *et al.* The intracellular sensor NLRP3 mediates key innate and healing responses to influenza A virus via the regulation of caspase-1. *Immunity* **30**, 566-575 (2009).
11. Cama, V.F. *et al.* The microglial NLRP3 inflammasome is involved in human SARS-CoV-2 cerebral pathogenicity: A report of three post-mortem cases. *J Neuroimmunol* **361**, 577728 (2021).
12. Eisfeld, H.S. *et al.* Viral Glycoproteins Induce NLRP3 Inflammasome Activation and Pyroptosis in Macrophages. *Viruses* **13** (2021).
13. Junqueira, C. *et al.* FcγR-mediated SARS-CoV-2 infection of monocytes activates inflammation. *Nature* (2022).
14. Sefik, E. *et al.* Inflammasome activation in infected macrophages drives COVID-19 pathology. *Nature* (2022).
15. Lucas, C.W., P. LKlein, J. et al. Longitudinal analyses reveal immunological misfiring in severe COVID-19. *Nature* (2020).
16. Rodrigues, T.S. *et al.* Inflammasomes are activated in response to SARS-CoV-2 infection and are associated with COVID-19 severity in patients. *J Exp Med* **218** (2021).
17. Kommoss, F.K.F. *et al.* The Pathology of Severe COVID-19-Related Lung Damage. *Dtsch Arztebl Int* **117**, 500-506 (2020).
18. Xu, Z. *et al.* Pathological findings of COVID-19 associated with acute respiratory distress syndrome. *Lancet Respir Med* **8**, 420-422 (2020).
19. Sauter, J.L. *et al.* Insights into pathogenesis of fatal COVID-19 pneumonia from histopathology with immunohistochemical and viral RNA studies. *Histopathology* **77**, 915-925 (2020).
20. Toldo, S. *et al.* Inflammasome formation in the lungs of patients with fatal COVID-19. *Inflamm Res* **70**, 7-10 (2021).
21. Taubenberger, J.K. & Morens, D.M. The pathology of influenza virus infections. *Annu Rev Pathol* **3**, 499-522 (2008).
22. Glass, G., Papin, J.A. & Mandell, J.W. SIMPLE: a sequential immunoperoxidase labeling and erasing method. *J Histochem Cytochem* **57**, 899-905 (2009).
23. Lu, X. *et al.* US CDC Real-Time Reverse Transcription PCR Panel for Detection of Severe Acute Respiratory Syndrome Coronavirus 2. *Emerg Infect Dis* **26**, 1654-1665 (2020).
24. Corman, V.M. *et al.* Detection of 2019 novel coronavirus (2019-nCoV) by real-time RT-PCR. *Euro surveillance : bulletin Europeen sur les maladies transmissibles = European communicable disease bulletin* **25** (2020).
25. Raghu, G. *et al.* Diagnosis of Idiopathic Pulmonary Fibrosis. An Official ATS/ERS/JRS/ALAT Clinical Practice Guideline. *American journal of respiratory and critical care medicine* **198**, e44-e68 (2018).
26. Koenigkam-Santos, M. *et al.* SARS-Cov-2 pneumonia phenotyping on imaging exams of patients submitted to minimally invasive autopsy. *Ann Transl Med* **10**, 140 (2022).
27. Revel, M.P. *et al.* COVID-19 patients and the radiology department - advice from the European Society of Radiology (ESR) and the European Society of Thoracic Imaging (ESTI). *Eur Radiol* **30**, 4903-4909 (2020).
28. Weibel, E.R. Principles and methods for the morphometric study of the lung and other organs. *Lab Invest* **12**, 131-155 (1963).

29. Hariri, L.P. *et al.* Lung Histopathology in Coronavirus Disease 2019 as Compared With Severe Acute Respiratory Sydrome and H1N1 Influenza: A Systematic Review. *Chest* **159**, 73-84 (2021).
30. Hauenstein, A.V., Zhang, L. & Wu, H. The hierarchical structural architecture of inflammasomes, supramolecular inflammatory machines. *Current opinion in structural biology* **31**, 75-83 (2015).
31. Weinheimer, V.K. *et al.* Influenza A viruses target type II pneumocytes in the human lung. *J Infect Dis* **206**, 1685-1694 (2012).
32. Sinha, P., Matthay, M.A. & Calfee, C.S. Is a "Cytokine Storm" Relevant to COVID-19?, in *JAMA Intern Med*, Vol. 180 1152-1154 (United States; 2020).
33. Peiris, J.S. *et al.* Re-emergence of fatal human influenza A subtype H5N1 disease. *Lancet* **363**, 617-619 (2004).
34. de Jong, M.D. *et al.* Fatal outcome of human influenza A (H5N1) is associated with high viral load and hypercytokinemia. *Nat Med* **12**, 1203-1207 (2006).
35. Kash, J.C. *et al.* Genomic analysis of increased host immune and cell death responses induced by 1918 influenza virus. *Nature* **443**, 578-581 (2006).
36. Cillóniz, C. *et al.* Lethal influenza virus infection in macaques is associated with early dysregulation of inflammatory related genes. *PLoS Pathog* **5**, e1000604 (2009).
37. Kobasa, D. *et al.* Aberrant innate immune response in lethal infection of macaques with the 1918 influenza virus. *Nature* **445**, 319-323 (2007).
38. Qin, C. *et al.* Dysregulation of Immune Response in Patients With Coronavirus 2019 (COVID-19) in Wuhan, China. *Clin Infect Dis* **71**, 762-768 (2020).
39. Chen, H. *et al.* SARS-CoV-2 activates lung epithelial cell proinflammatory signaling and leads to immune dysregulation in COVID-19 patients. *EBioMedicine* **70**, 103500 (2021).
40. Huang, K.J. *et al.* An interferon-gamma-related cytokine storm in SARS patients. *J Med Virol* **75**, 185-194 (2005).
41. Olajide, O.A., Iwuanyanwu, V.U., Lepiarz-Raba, I. & Al-Hindawi, A.A. Induction of Exaggerated Cytokine Production in Human Peripheral Blood Mononuclear Cells by a Recombinant SARS-CoV-2 Spike Glycoprotein S1 and Its Inhibition by Dexamethasone. *Inflammation* **44**, 1865-1877 (2021).
42. Cui, H. & Zhang, L. Key Components of Inflammasome and Pyroptosis Pathways Are Deficient in Canines and Felines, Possibly Affecting Their Response to SARS-CoV-2 Infection. *Front Immunol* **11**, 592622 (2020).
43. Dolinay, T. *et al.* Inflammasome-regulated cytokines are critical mediators of acute lung injury. *American journal of respiratory and critical care medicine* **185**, 1225-1234 (2012).
44. Taylor, F.B., Jr. *et al.* Towards definition, clinical and laboratory criteria, and a scoring system for disseminated intravascular coagulation. *Thromb Haemost* **86**, 1327-1330 (2001).
45. Taniguchi, Y. *et al.* Comparison of patient characteristics and in-hospital mortality between patients with COVID-19 in 2020 and those with influenza in 2017-2020: a multicenter, retrospective cohort study in Japan. *Lancet Reg Health West Pac* **20**, 100365 (2022).
46. Fröhlich, G.M. *et al.* Hospital outcomes of community-acquired COVID-19 versus influenza: Insights from the Swiss hospital-based surveillance of influenza and COVID-19. *Euro surveillance : bulletin Europeen sur les maladies transmissibles = European communicable disease bulletin* **27** (2022).
47. Godaert, L., Cebille, A., Proye, E. & Dramé, M. COVID-19 versus Seasonal Influenza: Comparison of Profiles of Older Adults Hospitalized in a Short-Term Geriatric Ward in France. *Am J Trop Med Hyg* **106**, 108-113 (2021).
48. Manzanares-Meza, L.D. & Medina-Contreras, O. SARS-CoV-2 and influenza: a comparative overview and treatment implications. *Bol Med Hosp Infant Mex* **77**, 262-273 (2020).
49. Ogiwara, H. *et al.* Histopathological evaluation of the diversity of cells susceptible to H5N1 virulent avian influenza virus. *Am J Pathol* **184**, 171-183 (2014).
50. Ramos da Silva, S. *et al.* Broad Severe Acute Respiratory Syndrome Coronavirus 2 Cell Tropism and Immunopathology in Lung Tissues From Fatal Coronavirus Disease 2019. *J Infect Dis* **223**, 1842-1854 (2021).
51. Bhatnagar, J. *et al.* Evidence of Severe Acute Respiratory Syndrome Coronavirus 2 Replication and Tropism in the Lungs, Airways, and Vascular Endothelium of Patients With Fatal Coronavirus Disease 2019: An Autopsy Case Series. *J Infect Dis* **223**, 752-764 (2021).
52. Pei, R. *et al.* Host metabolism dysregulation and cell tropism identification in human airway and alveolar organoids upon SARS-CoV-2 infection. *Protein Cell* **12**, 717-733 (2021).
53. Park, H.S. *et al.* NS1 Protein of 2009 Pandemic Influenza A Virus Inhibits Porcine NLRP3 Inflammasome-Mediated Interleukin-1 Beta Production by Suppressing ASC Ubiquitination. *J Virol* **92** (2018).
54. Ichinohe, T., Lee, H.K., Ogura, Y., Flavell, R. & Iwasaki, A. Inflammasome recognition of influenza virus is essential for adaptive immune responses. *J Exp Med* **206**, 79-87 (2009).
55. Schmitz, N., Kurrer, M., Bachmann, M.F. & Kopf, M. Interleukin-1 is responsible for acute lung immunopathology but increases survival of respiratory influenza virus infection. *J Virol* **79**, 6441-6448 (2005).

696 56. Broz, P. & Dixit, V.M. Inflammasomes: mechanism of assembly, regulation and signalling.
697 *Nat Rev Immunol* **16**, 407-420 (2016).
698 57. Delorey, T.M. *et al.* COVID-19 tissue atlases reveal SARS-CoV-2 pathology and cellular
699 targets. *Nature* **595**, 107-113 (2021).
700 58. Pontelli, M.C. *et al.* SARS-CoV-2 productively infects primary human immune system cells in
701 vitro and in COVID-19 patients. *J Mol Cell Biol* (2022).
702 59. Ji, J., Hou, J., Xia, Y., Xiang, Z. & Han, X. NLRP3 inflammasome activation in alveolar
703 epithelial cells promotes myofibroblast differentiation of lung-resident mesenchymal stem
704 cells during pulmonary fibrogenesis. *Biochim Biophys Acta Mol Basis Dis* **1867**, 166077
705 (2021).
706 60. Furukawa, S., Matsuda, K., Sugano, M., Uehara, T. & Honda, T. NLRP3 upregulation in
707 A549 cells co-cultured with THP-1 macrophages under hypoxia via deregulated TGF-β
708 signaling. *Exp Cell Res* **383**, 111506 (2019).
709 61. Wang, Y. *et al.* Activation of NLRP3 inflammasome enhances the proliferation and migration
710 of A549 lung cancer cells. *Oncol Rep* **35**, 2053-2064 (2016).
711 62. Schimmel, L. *et al.* Endothelial cells are not productively infected by SARS-CoV-2. *Clin*
712 *Transl Immunology* **10**, e1350 (2021).
713 63. Ratajczak, M.Z. *et al.* SARS-CoV-2 Entry Receptor ACE2 Is Expressed on Very Small
714 CD45(-) Precursors of Hematopoietic and Endothelial Cells and in Response to Virus Spike
715 Protein Activates the Nlrp3 Inflammasome. *Stem Cell Rev Rep* **17**, 266-277 (2021).
716 64. Kucia, M. *et al.* An evidence that SARS-Cov-2/COVID-19 spike protein (SP) damages
717 hematopoietic stem/progenitor cells in the mechanism of pyroptosis in Nlrp3 inflammasome-
718 dependent manner. *Leukemia*, 1-4 (2021).
719 65. Xiang, M. *et al.* Hemorrhagic shock activation of NLRP3 inflammasome in lung endothelial
720 cells. *J Immunol* **187**, 4809-4817 (2011).
721 66. Xu, P. *et al.* Hemorrhagic shock augments Nlrp3 inflammasome activation in the lung
722 through impaired pyrin induction. *J Immunol* **190**, 5247-5255 (2013).
723 67. Yang, J. *et al.* Hemorrhagic shock primes for lung vascular endothelial cell pyroptosis: role in
724 pulmonary inflammation following LPS. *Cell Death Dis* **7**, e2363 (2016).
725 68. Paul, O. *et al.* Vascular Inflammation in Lungs of Patients with Fatal Coronavirus Disease
726 2019 (COVID-19) Infection: Possible role for the NLRP3 inflammasome. *medRxiv* (2021).
727 69. Hottz, E.D. *et al.* Platelet activation and platelet-monocyte aggregate formation trigger tissue
728 factor expression in patients with severe COVID-19. *Blood* **136**, 1330-1341 (2020).
729 70. Varga, Z. *et al.* Endothelial cell infection and endotheliitis in COVID-19. *Lancet* **395**, 1417-
730 1418 (2020).
731 71. Liu, J. *et al.* SARS-CoV-2 cell tropism and multiorgan infection, in *Cell Discov*, Vol. 7 17
732 (2021).
733 72. Nuovo, G.J. *et al.* Endothelial cell damage is the central part of COVID-19 and a mouse
734 model induced by injection of the S1 subunit of the spike protein. *Annals of diagnostic*
735 *pathology* **51**, 151682 (2021).
736 73. Ward, S.E. *et al.* Von Willebrand factor propeptide in severe coronavirus disease 2019
737 (COVID-19): evidence of acute and sustained endothelial cell activation. *Br J Haematol* **192**,
738 714-719 (2021).
739 74. Libby, P. & Lüscher, T. COVID-19 is, in the end, an endothelial disease. *Eur Heart J* **41**,
740 3038-3044 (2020).
741 75. Wu, C. *et al.* Inflammasome Activation Triggers Blood Clotting and Host Death through
742 Pyroptosis. *Immunity* **50**, 1401-1411.e1404 (2019).
743 76. Campos, J. *et al.* Neutrophil extracellular traps and inflammasomes cooperatively promote
744 venous thrombosis in mice. *Blood Adv* **5**, 2319-2324 (2021).
745 77. Zhang, Y. *et al.* Inflammasome activation promotes venous thrombosis through pyroptosis.
746 *Blood Adv* **5**, 2619-2623 (2021).
747 78. Hussain, S. *et al.* Inflammasome activation in airway epithelial cells after multi-walled carbon
748 nanotube exposure mediates a profibrotic response in lung fibroblasts. *Part Fibre Toxicol* **11**,
749 28 (2014).
750 79. Meng, Y. *et al.* The angiotensin-converting enzyme 2/angiotensin (1-7)/Mas axis protects
751 against lung fibroblast migration and lung fibrosis by inhibiting the NOX4-derived ROS-
752 mediated RhoA/Rho kinase pathway. *Antioxid Redox Signal* **22**, 241-258 (2015).
753 80. Meng, Y. *et al.* Autophagy Attenuates Angiotensin II-Induced Pulmonary Fibrosis by
754 Inhibiting Redox Imbalance-Mediated NOD-Like Receptor Family Pyrin Domain Containing 3
755 Inflammasome Activation. *Antioxid Redox Signal* **30**, 520-541 (2019).
756 81. Sun, B. *et al.* Repetitive Dosing of Fumed Silica Leads to Profibrogenic Effects through
757 Unique Structure-Activity Relationships and Biopersistence in the Lung. *ACS Nano* **10**,
758 8054-8066 (2016).
759 82. Cho, S.J. *et al.* GLUT1-dependent glycolysis regulates exacerbation of fibrosis via AIM2
760 inflammasome activation. *Thorax* **75**, 227-236 (2020).

761 83. Lv, Z. *et al.* NLRP3 Inflammasome Activation Contributes to Mechanical Stretch-Induced
762 Endothelial-Mesenchymal Transition and Pulmonary Fibrosis. *Crit Care Med* **46**, e49-e58
763 (2018).
764 84. Postlethwaite, A.E. *et al.* Modulation of fibroblast functions by interleukin 1: increased
765 steady-state accumulation of type I procollagen messenger RNAs and stimulation of other
766 functions but not chemotaxis by human recombinant interleukin 1 alpha and beta. *J Cell Biol*
767 **106**, 311-318 (1988).
768 85. Walsh, K.A. *et al.* SARS-CoV-2 detection, viral load and infectivity over the course of an
769 infection. *J Infect* **81**, 357-371 (2020).
770 86. Desai, N. *et al.* Temporal and Spatial Heterogeneity of Host Response to SARS-CoV-2
771 Pulmonary Infection. *medRxiv* (2020).
772 87. Jones, H.D. *et al.* The NLRP3 inflammasome is required for the development of hypoxemia
773 in LPS/mechanical ventilation acute lung injury. *Am J Respir Cell Mol Biol* **50**, 270-280
774 (2014).
775 88. Zhang, Y., Liu, G., Dull, R.O., Schwartz, D.E. & Hu, G. Autophagy in pulmonary
776 macrophages mediates lung inflammatory injury via NLRP3 inflammasome activation during
777 mechanical ventilation. *Am J Physiol Lung Cell Mol Physiol* **307**, L173-185 (2014).
778 89. Kuipers, M.T. *et al.* Ventilator-induced lung injury is mediated by the NLRP3 inflammasome.
779 *Anesthesiology* **116**, 1104-1115 (2012).
780 90. Kolliputi, N., Shaik, R.S. & Waxman, A.B. The inflammasome mediates hyperoxia-induced
781 alveolar cell permeability. *J Immunol* **184**, 5819-5826 (2010).
782 91. Wu, J. *et al.* Activation of NLRP3 inflammasome in alveolar macrophages contributes to
783 mechanical stretch-induced lung inflammation and injury. *J Immunol* **190**, 3590-3599 (2013).

784

785 **Table 1**. Influenza and COVID-19 patients characteristics

Demographic Characteristics	Influenza Mean (±SD) or N (%)	SARS-CoV-2 Mean (±SD) or N (%)	p value
N	12	47	
Sex			
Female	4 (33.33%)	23 (48.93%)	0.5177*
Male	8 (66.66%)	24 (51.06%)	
Age (years)	41.5 (15.24±)	67.97 (15.05±)	<0.0001**
Illness Time (days)	-	18.08 (11.04±)	-
ICU	4 (33.33%)	37 (78.72%)	0.0045*
Influenza A (H1N1)	5 (41.66%)	-	-
Influenza A (H3N2)	2 (16.66%)	-	-
Influenza A not subtyped	3 (25.00%)	-	-
Influenza B	2 (16.66%)	-	-
Comorbidities			
Hypertension	2 (16.66%)	26 (55.32%)	0.0233*
BMI	-	31.10 (±8.82)	-
Diabetes	3 (25.00%)	18 (38.29%)	0.5092*
History of smoking	0 (0.00%)	12 (25.53%)	0.1012*
Heart disease	2 (16.66%)	12 (25.53%)	0.7119*
Lung disease	1 (8.33%)	12 (25.53%)	0.2679*
Kidney disease	0 (0.00%)	7 (14.89%)	0.3255*
History of stroke	0 (0.00%)	7 (14.89%)	0.3255*
Autoimmune diseases	0 (0.00%)	2 (4.25%)	>0.9999*
Laboratorial findings			
CRP (mg/dL)	22.55 (±12.66)	11.40 (±8.49)	0.0061**
D-Dimers (µg/mL)	-	4.91 (±4.46)	-
LDH (mmol/L)	5.18 (±3.91)	5.01 (±5.24)	0.9443**
Creatinine (mg/dL)	4.59 (±2.41)	2.22 (±1.4)	0.0008**
Urea (mg/dL)	140 (±64.07)	119.40 (±58.47)	0.4247**
AST (IU/L)	228 (±235.06)	104.42 (±90.74)	0.0174**
ALT (IU/L)	38.2 (±32.12)	72.12 (±55.14)	0.2012**
AST/ALT	3.99 (±2.66)	1.8 (±1.60)	0.0115**
PT (INR)	1.44 (±0.65)	1.81 (±2.13)	0.6765**
Albumin (g/dL)	3.02 (±1.36)	3.09 (±0.58)	0.8327**
Blood Glucose (mg/dL)	181.2 (±105.58)	194.72 (±94.60)	0.7656**
Respiratory status			
Temperature (ºC)	38.14 (±2.58)	37.39 (±1.73)	0.3833**
Mechanical ventilation	-	36 (76.59%)	-
Nasal-cannula oxygen	4 (33.33%)	11 (23.40%)	>0.9999*
Intubated time (days)	0.30 (±0.57)	12.38 (±7.14)	0.0004**
P_aO_2 (mmHg)	103.61 (±35.98)	74.01 (±24.63)	0.0112**
Venous saturation (S_vO_2)	74.54 (±9.23)	67.58 (±25.34)	0.5477**
P_aO_2/FiO_2#	476.85 (±257.13)	159.69 (±90.84)	<0.0001**
A-a O_2 Gradient Value#	157.73 (±294.00)	283.22 (±208.31)	0.3988**
Respiratory Rate (mov/min)	24.40 (±9.07)	26.55 (±6.80)	0.4764**
Histopathological findings			
Fibrosis (% of area)	1.66 (±5.77)	30.00 (±12.68)	<0.0001**
Organizing Pneumonia (% of area)	4.16 (±14.43)	10.74 (±14.89)	0.0437**
Acute Fibrinous and Organizing Pneumonia (% of area)	8.33 (±15.27)	6.91 (±12.49)	0.9052**
Diffuse Alveolar Damage (% of area)	37.5 (±37.44)	17.87 (±21.05)	0.1419**
Pneumonitis (% of area)	1.66 (±3.89)	22.57 (±15.34)	<0.0001**
Pulmonary infarction (% of area)	8.33 (±13.37)	3.404 (±9.618)	0.1363**

786 * Fisher's exact test; ** t-Test; # data after 18 days of hospitalization.

787 **Table 2**. COVID-19 (Cluster 1 and Cluster 2) patients characteristics

Demographic Characteristics	Cluster 1 Mean (±SD) or N (%)	Cluster 2 Mean (±SD) or N (%)	p value
N	16	31	-
Sex			
Female	6 (37.50%)	17 (54.83%)	0.358*
Male	10 (62.50%)	14 (45.16%)	
Age (years)	70.81 (±10.34)	66.5 (±17.46)	0.369**
Illness Time (days)	12.06 (±6.97)	21.19 (±9.64)	0.001**
ICU	11 (68.75%)	25 (80.64%)	0.471*
Comorbidities			
Hypertension	10 (62.50%)	16 (51.61%)	0.546*
BMI	28.39 (±6.92)	33.21 (±8.52)	0.057**
Diabetes	7 (43.75%)	11 (35.48%)	0.999*
History of smoking	4 (25.00%)	8 (25.80%)	0.999*
Heart disease	4 (25.00%)	8 (25.80%)	0.999*
Lung disease	3 (18.75%)	9 (29.03%)	0.505*
Kidney disease	1 (6.25%)	6 (19.35%)	0.395*
History of stroke	3 (18.75%)	4 (12.90%)	0.675*
Autoimmune diseases	1 (6.25%)	1 (3.22%)	0.999*
Laboratorial findings			
CRP (mg/dL)	11.54 (±1.64)	11.32 (±9.15)	0.924**
D-Dimers (µg/mL)	6.07 (±5.45)	4.38 (±3.91)	0.227**
LDH (mmol/L)	6.17 (±6.42)	4.41 (±4.52)	0.280**
Creatinine (mg/dL)	2.41 (±1.64)	2.12 (±1.21)	0.494**
Urea (mg/dL)	108.36 (±53.92)	125.09 (±60.75)	0.358**
AST (IU/L)	110.65 (±112.67)	101.08 (±78.69)	0.735**
ALT (IU/L)	72.40 (±59.92)	71.98 (±53.88)	0.980**
AST/ALT	2.1 (±2.47)	1.6 (±0.92)	0.319**
PT (INR)	1.56 (±0.98)	1.95 (±2.55)	0.560**
Albumin (g/dL)	3.24 (±0.65)	3.01 (±0.54)	0.251**
Blood Glucose (mg/dL)	191.00 (±100.25)	196.65 (±96.32)	0.851**
Respiratory status			
Temperature (ºC)	37.74 (±1.82)	37.20 (±1.62)	0.304**
Mechanical ventilation	11 (68.75%)	25 (80.64%)	0.471*
Nasal-cannula oxygen	5 (31.25%)	6 (19.35%)	0.471*
Intubated time (days)	8 (±4.72)	14.32 (±6.94)	0.009**
P_aO_2 (mmHg)	75.54 (±8.06)	73.27 (±1.69)	0.135**
Venous saturation (S_vO_2)	61.33 (±27.83)	70.59 (±19.27)	0.187**
P_aO_2/FiO_2#	216.16 (±32.94)	164.15 (±21.09)	<0.001**
A-a O_2 Gradient Value#	40.20 (±101.48)	237.58 (±68.05)	0.006**
Respiratory Rate (mov/min)	26.76 (±7.86)	26.45 (±5.75)	0.878**
Histopathological findings, vascular status and Inflammasome activation			
Fibrosis (% of area)	24.38 (±11.59)	32.90 (±14.05)	0.042**
Organizing Pneumonia (% of area)	23.30 (±18.16)	24.50 (±15.71)	0.815**
Acute Fibrinous and Organizing Pneumonia (% of area)	18.33 (±12.24)	23.89 (±15.76)	0.225**
Diffuse Alveolar Damage (% of area)	34.00 (±24.03)	33.33 (±20.23)	0.920**
Pneumonitis (% of area)	20.67 (±18.52)	23.86 (±15.88)	0.540**
Pulmonary infarction (% of area)	26.67 (±14.14)	20.00 (±14.14)	0.132**
Disseminated Intravascular Coagulation	8 (50.00%)	5 (16.13%)	0.0198*
NLRP3 puncta per parenchyma area (mm^2)	143.67 (±89.00)	238.40 (±157.76)	0.031**

788 * Fisher's exact test; ** t-Test; # data after 18 days of hospitalization.

789

Table 3. Radiological Analyzes

	Cluster 1	Cluster 2	P value
Initial CXR pattern			
No opacities	1 (6.250%)	3 (9.67%)	0.9101
Mild viral pneumonia	2 (12.50%)	3 (9.67%)	
Moderate viral pneumonia	8 (50.00%)	12 (38.70%)	
Severe viral pneumonia	5 (31.25%)	11 (35.48%)	
Impaired analysis	0	2 (6.45%)	
Last CXR pattern			
No opacities	1 (6.25%)	2 (6.45%)	0.9971
Mild viral pneumonia	3 (18.75%)	5 (16.12%)	
Moderate viral pneumonia	6 (37.50%)	12 (38.70%)	
Severe viral pneumonia	4 (25.00%)	8 (25.80%)	
Impaired analysis	2 (12.50%)	4 (12.90%)	
Imaging evolution until death			
Improvement (fewer opacities)	5 (33.33%)	10 (32.25%)	0.0364
Stability	7 (46.66%)	4 (12.90%)	
Worsening (more opacities)	2 (13.33%)	12 (38.70%)	
Impaired analysis	1 (6.66%)	5 (16.12%)	
Disease Extent (Thoracic CT)			
0	0	0	0.0363
<25%	4 (66.66%)	1 (12.50%)	
25-50%	0	3 (37.50%)	
50-75%	1 (16.66%)	3 (37.50%)	
>75%	1 (16.66%)	1 (12.50%)	

806 **Table 4**. Characteristics of covid-19 patients who were submitted or not to mechanical
807 ventilation (MV).

Demographics Characteristics	**MV+** Mean (±SD) or N (%)	**MV-** Mean (±SD) or N (%)	**p value**
N	36	11	
Sex			
Female	17 (47.22%)	6 (54.54%)	0.7400*
Male	19 (52.77%)	5 (45.45%)	
Age (years)	65.61 (±13.52)	75.72 (±17.61)	0.0493**
Illness Time (days)	20.94 (±10.76)	8.72 (±5.40)	0.0007**
ICU	36 (100.00%)	0 (0.00%)	>0.9999*
Comorbidities			
Hypertension	23 (63.88%)	3 (27.27%)	0.0433*
BMI	30.61 (±8.52)	34.56 (±14.46)	0.4324**
Diabetes	16 (44.44%)	2 (18.18%)	0.1644*
History of smoking	11 (30.55%)	3 (27.77%)	>0.9999*
Heart disease	11 (30.55%)	1 (9.09%)	0.2440*
Lung disease	9 (25.00%)	2 (18.18%)	>0.9999*
Kidney disease	6 (16.66%)	1 (9.09%)	>0.9999*
History of stroke	4 (11.11%)	3 (27.77%)	0.3296*
Autoimmune diseases	1 (2.77%)	1 (9.09%)	0.4172*
Laboratorial findings			
CRP (mg/dL)	9.99 (±7.83)	16.02 (±9.29)	0.0377**
D-Dimers (µg/mL)	4.99 (±4.68)	4.56 (±3.62)	0.7989**
LDH (mmol/L)	5.78 (±5.76)	2.49 (±1.13)	0.0680**
Creatinine (mg/dL)	1.58 (±1.39)	1.05 (±0.50)	0.2242**
Urea (mg/dL)	138.18 (±54.07)	64.48 (±34.12)	0.0001**
AST (IU/L)	109.61 (±98.16)	84.81 (±54.14)	0.4725**
ALT (IU/L)	79.02 (±58.67)	45.38 (±26.97)	0.1254**
AST/ALT	1.6 (±1.74)	2.2 (±0.88)	0.3542**
PT (INR)	1.53 (±0.91)	2.82 (±4.24)	0.0900**
Albumin (g/dL)	2.99 (±0.54)	3.78 (±0.41)	0.0034**
Blood Glucose (mg/dL)	198.22 (±93.77)	181.11 (±102.34)	0.6340**
Respiratory status			
Temperature (ºC)	37.51 (±1.79)	36.99 (±1.53)	0.3890**
P_aO_2 (mmHg)	79.57 (±20.19)	53.99 (±24.12)	0.0014**
Venous saturation (S_vO_2)	70.86 (±14.36)	50.71 (±31.26)	0.0092**
P_aO_2/FiO_2#	132.63 (±67.94)	257.11 (±114.86)	<0.0001**
A-a O_2 Gradient Value#	351.09 (±183.40)	45.69 (±26.55)	<0.0001**
Respiratory Rate (mov/min)	27.61 (±6.17)	23.09 (±7.89)	0.0669**
Histopathological findings			
Fibrosis (% of area)	30.28 (±14.05)	29.09 (±12.21)	0.8015**
Organizing Pneumonia (% of area)	26.11 (±13.56)	20.00 (±11.54)	0.4520**
Acute Fibrinous and Organizing Pneumonia (% of area)	19.50 (±12.48)	26.00 (±15.16)	0.3906**
Diffuse Alveolar Damage (% of area)	28.82 (±19.34)	43.75 (±16.85)	0.0742**
Pneumonitis (% of area)	23.52 (±17.33)	20.00 (±8.16)	0.5435**
Pulmonary infarction (% of area)	25.00 (±10.00)	10.00 (±0.00)	0.2235**
Inflammasome activation			
NLRP3 puncta per parenchyma area (mm²)	204.3 (±155.5)	204.0 (±156.6)	0.9310**
ASC puncta per parenchyma area (mm²)	251.8 (±192.5)	267.3 (±133.1)	0.4196**

808 * Fisher's exact test; ** t-Test; # data after 18 days of hospitalization.
809

Figures and Figure Legends

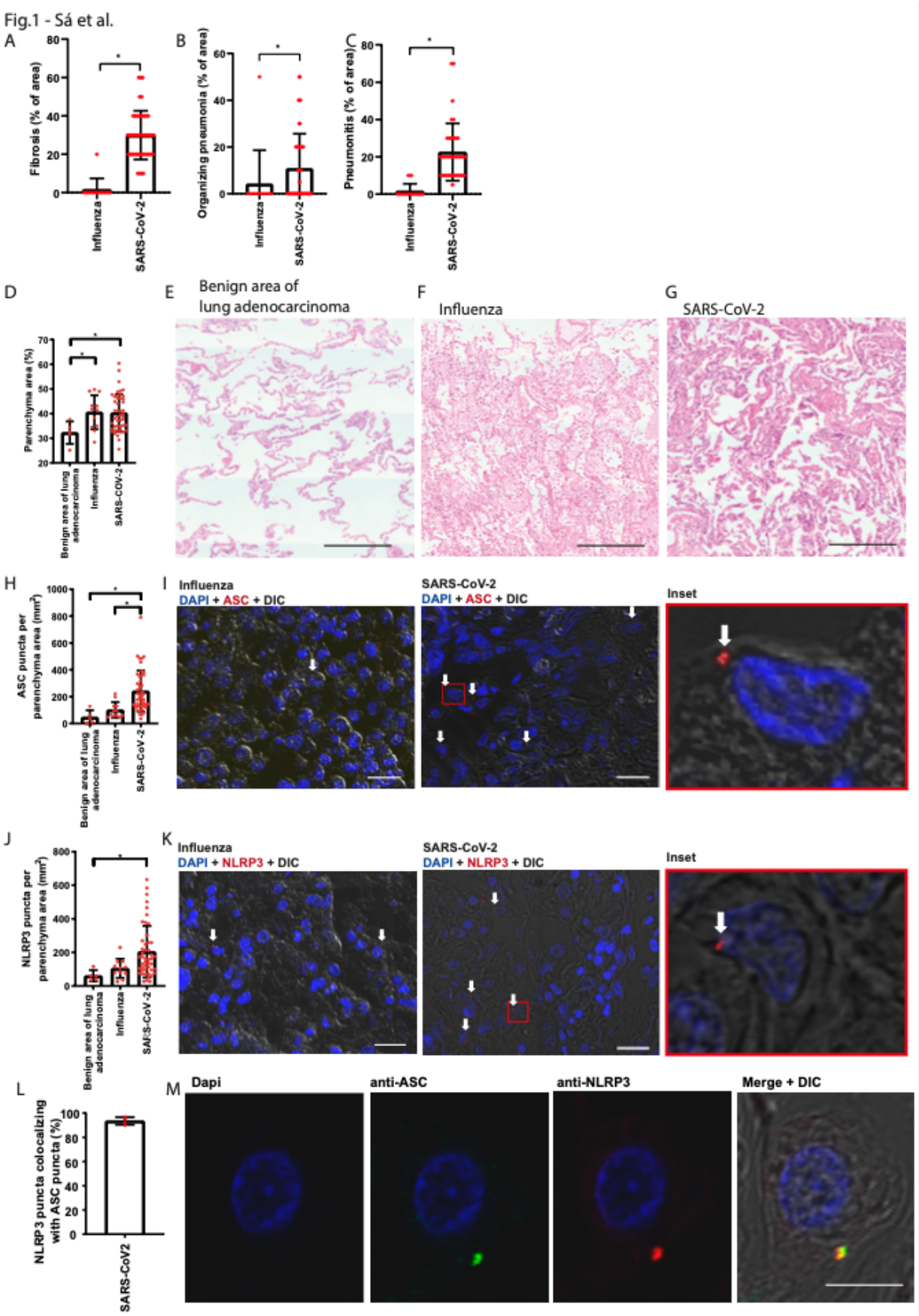

814

815

816 **Figure 1. Histopathological patterns and inflammasome activation in lung**
817 **autopsy of COVID-19 and influenza patients.** Histopathological analysis of lethal
818 cases of COVID-19 and Influenza patients. (**A-G**) Histological analysis of hematoxylin
819 and eosin (H&E) stained slides for the presence of fibrosis (**A**), organizing pneumonia
820 (**B**) and pneumonitis (**C**). (**D-G**) Proportion of lung parenchyma area of COVID-19,
821 Influenza and adenocarcinoma (benign area of the lungs) patients. (**E-G**)
822 Representative images of H&E stain showing the lung parenchyma. Scale bars 200
823 μm. (**H-K**) Multiphoton microscopy analysis of lung autopsies of 47 COVID-19 patients,
824 12 influenza patients and 5 lung adenocarcinoma patients. Tissues were stained with
825 anti-ASC (**H, I**) or anti-NLRP3 (**J, K**) for quantification of cells with inflammasome
826 puncta in lung autopsies (in red, indicated by white arrows). DAPI stains cell nuclei
827 (blue). Insets indicate a higher magnification of the indicated region (red rectangle).
828 Scale bars 20 μm. (**L**) Percentage of NLRP3 and ASC puncta colocalization in the
829 lungs of five COVID-19 patients. (**M**) Representative images showing ASC (green) and
830 NLRP3 (red) colocalization. Scale bar 10 μm. Each dot in the figure represents the
831 value obtained from each individual. *, $P < 0.05$ comparing the indicated groups, as
832 determined by Mann-Whitney test (**A-D**) or by Kruskal-Wallis test (**H, J**). The images
833 were acquired by multiphoton microscope using a 63x oil immersion objective and
834 analyzed using ImageJ Software.

835

Fig.2- Sá et al.

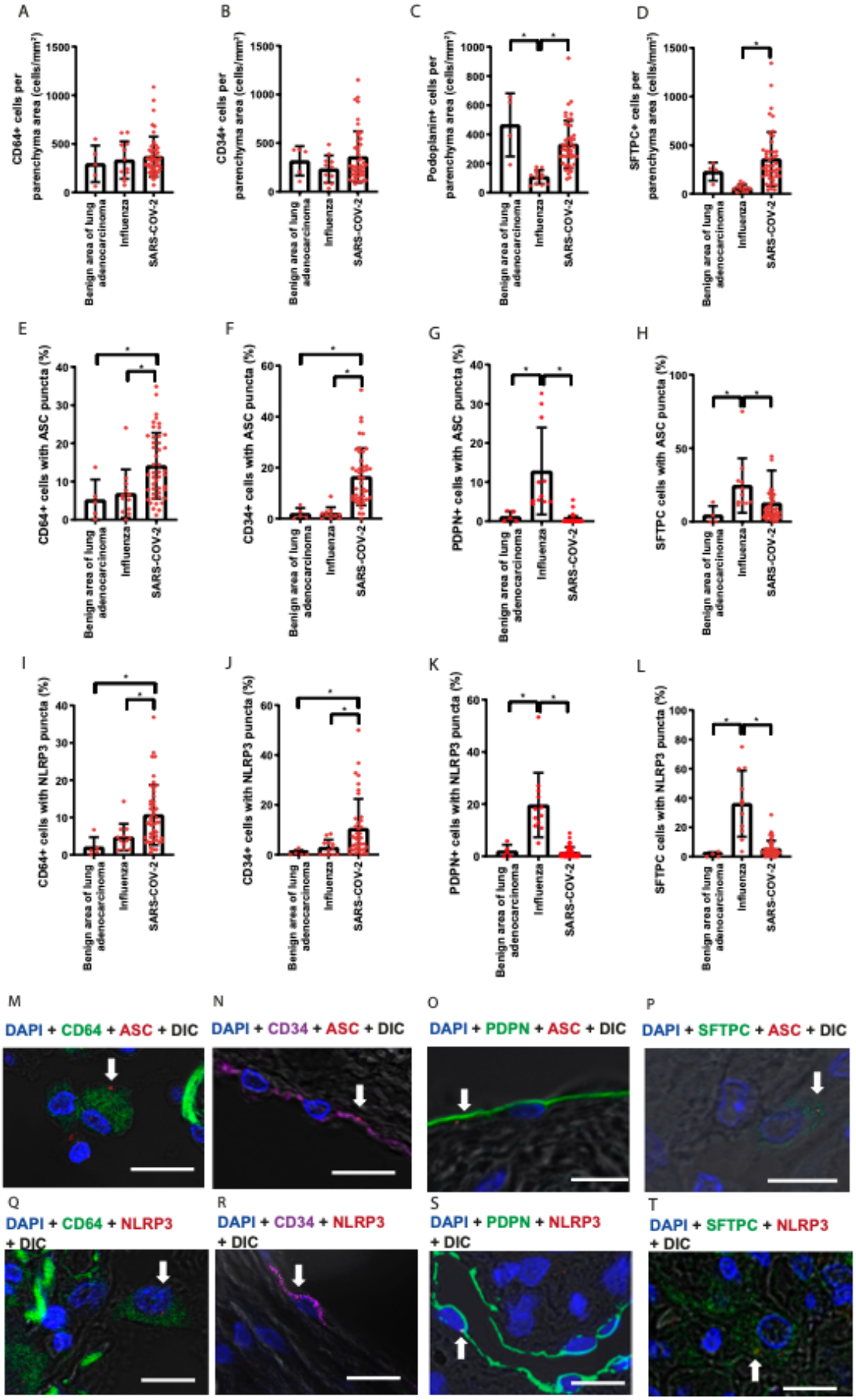
A
CD64+ cells per parenchyma area (cells/mm²)
B
CD34+ cells per parenchyma area (cells/mm²)
C
Podoplanin+ cells per parenchyma area (cells/mm²)
D
SFTPC+ cells per parenchyma area (cells/mm²)
E
CD64+ cells with ASC puncta (%)
F
CD34+ cells with ASC puncta (%)
G
PDPN+ cells with ASC puncta (%)
H
SFTPC cells with ASC puncta (%)
I
CD64+ cells with NLRP3 puncta (%)
J
CD34+ cells with NLRP3 puncta (%)
K
PDPN+ cells with NLRP3 puncta (%)
L
SFTPC cells with NLRP3 puncta (%)
Benign area of lung adenocarcinoma
Influenza
SARS-COV-2
M
DAPI + CD64 + ASC + DIC
N
DAPI + CD34 + ASC + DIC
O
DAPI + PDPN + ASC + DIC
P
DAPI + SFTPC + ASC + DIC
Q
DAPI + CD64 + NLRP3 + DIC
R
DAPI + CD34 + NLRP3 + DIC
S
DAPI + PDPN + NLRP3 + DIC
T
DAPI + SFTPC + NLRP3 + DIC

839

840

841 **Figure 2. Macrophages, endothelial cells, and pneumocytes contribute to**
842 **inflammasome activation in the lungs of COVID-19 patients and influenza**.
843 Multiphoton microscopy analysis of lung autopsies of 47 COVID-19 patients, 12
844 influenza patients and 5 lung adenocarcinoma patients (benign area of the lungs). (**A-**
845 **D**) Numbers of macrophages ($CD64^+$, **A**), endothelial cells ($CD34^+$, **B**), type I
846 pneumocytes ($PDPN^+$, **C**) and type II pneumocytes ($SFTPC^+$, **D**) per lung parenchyma
847 area. (**E-L**) Percentage $CD64^+$ (**E, I**), $CD34^+$ (**F, J**), $PDPN^+$ (**G, K**) and $SFTPC^+$ (**H, L**)
848 containing ASC (**E-H**) or NLRP3 (**I-L**) puncta. Each dot in the figures represents the
849 value obtained from each individual. *, $P < 0.05$ comparing the indicated groups, as
850 determined by Kruskal-Wallis test. (**M-T**) Representative image of ASC (**M-P**) or
851 NLRP3 (**Q-T**) puncta (in red; indicated by white arrows) in $CD64^+$ (in red; **M, Q**), $CD34^+$
852 (in purple; **N, R**), $PDPN^+$ (in green; **O, S**) and $SFTPC^+$ (in green; **P, T**) cells from a lung
853 autopsy of a COVID-19 patient. DAPI stains cell nuclei (blue). Scale bars 10 μm. The
854 images were acquired by multiphoton microscopy using a 63x oil immersion objective
855 and analyzed using ImageJ Software.

856

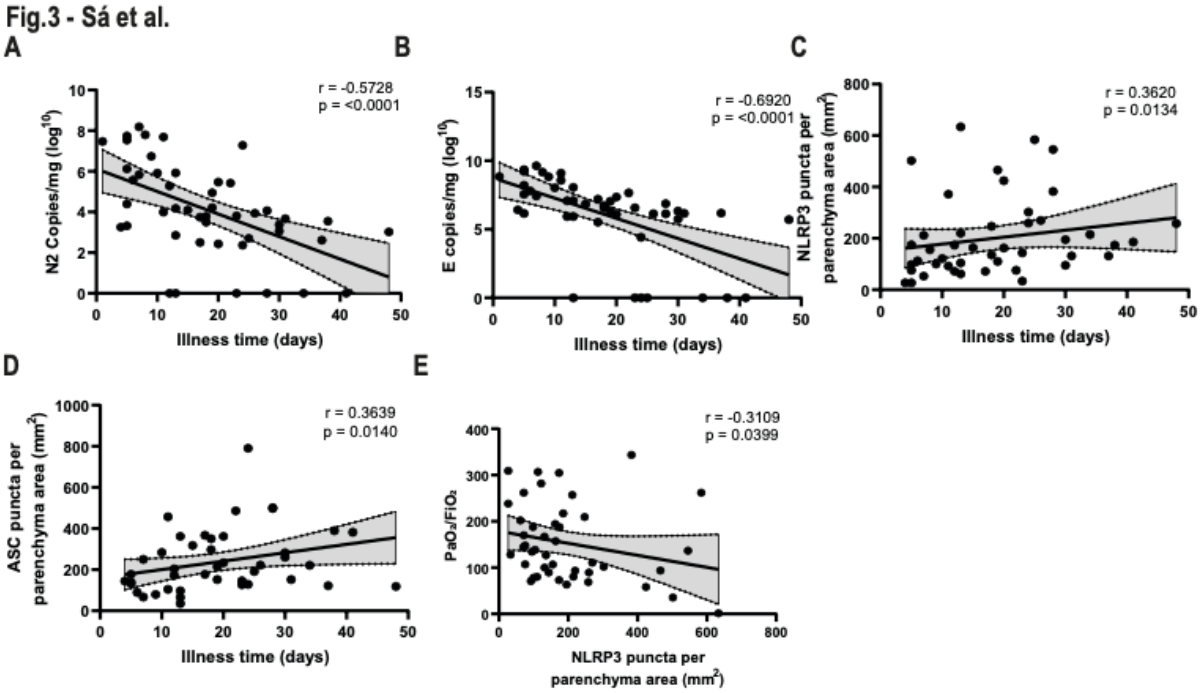

Figure 3. Inflammasome activation positively correlates with disease time, and viral load inversely correlates with disease time. Spearman correlation of pulmonary viral load, inflammasome activation and illness time in 47 fatal COVID-19 patients. (**A**) Correlation of viral N2 with illness time; (**B**) Correlation of viral E with illness time; (**C**) Correlation of NLRP3 puncta per parenchyma area with illness time; (**D**) Correlation of ASC puncta per parenchyma area with illness time; (**E**) Correlation of NLRP3 puncta per parenchyma area with PaO_2/FiO_2. r and p-value are indicated in the figure.

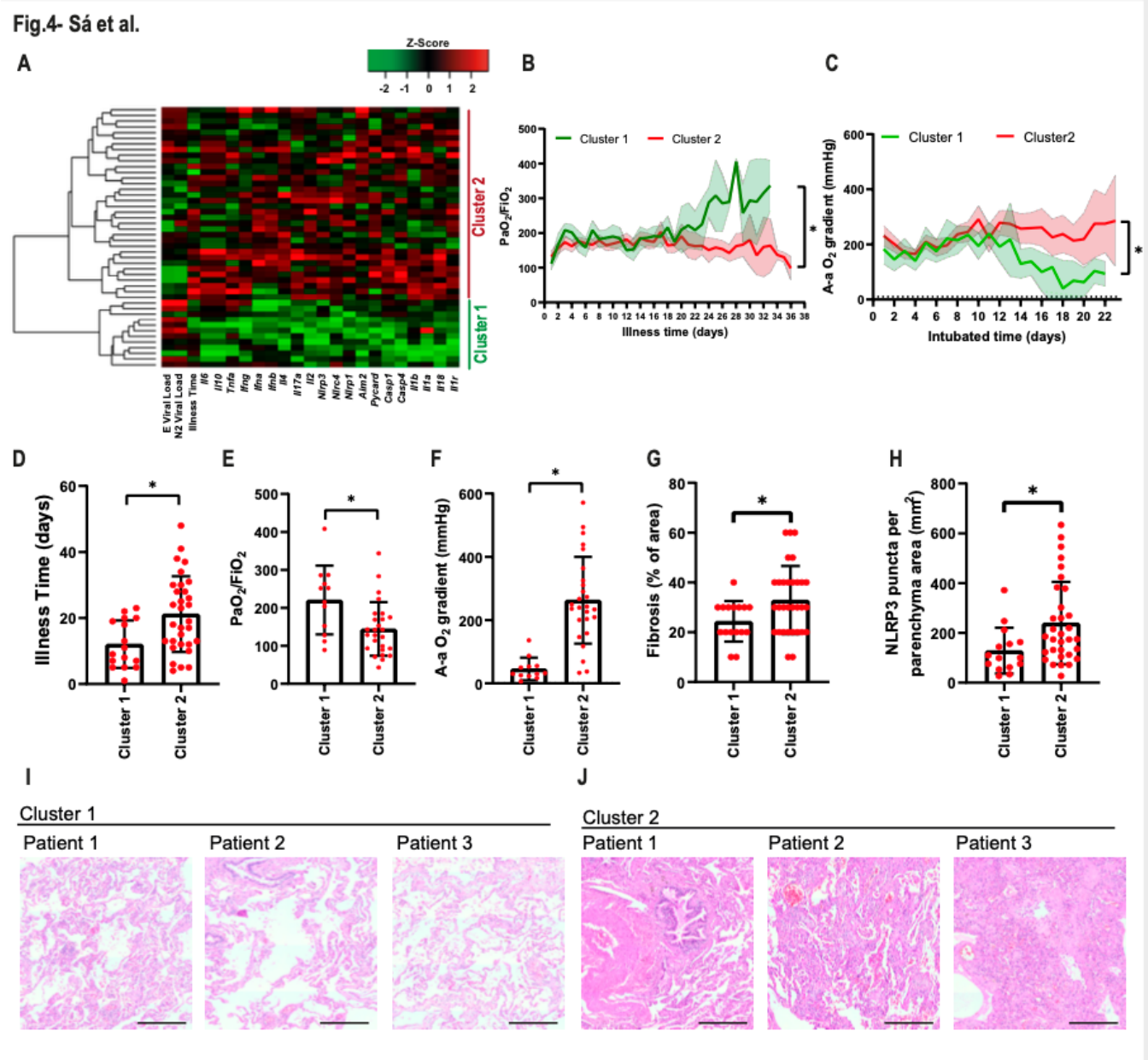
Fig.4- Sá et al.
A
Z-Score
-2 -1 0 1 2
Cluster 2
Cluster 1
E Viral Load
N2 Viral Load
Illness Time
Il6
Il10
Tnfa
Ifng
Ifna
Ifnb
Il4
Il17a
Il2
Nlrp3
Nlrc4
Nlrp1
Aim2
Pycard
Casp1
Casp4
Il1b
Il1a
Il18
Il1r
B
Cluster 1
Cluster 2
PaO2/FiO2
Illness time (days)
C
Cluster 1
Cluster2
A-a O2 gradient (mmHg)
Intubated time (days)
D
Illness Time (days)
E
PaO2/FiO2
F
A-a O2 gradient (mmHg)
G
Fibrosis (% of area)
H
NLRP3 puncta per parenchyma area (mm2)
Cluster 1
Cluster 2
I
Cluster 1
Patient 1
Patient 2
Patient 3
J
Cluster 2
Patient 1
Patient 2
Patient 3

876

877

878 **Figure 4. Pulmonary viral load and inflammatory gene expression defines two**
879 **patient clusters in lethal cases of COVID-19.** (**A**) Heatmap of the mRNA expression
880 of inflammasome, inflammatory molecules/cytokines and viral N2 and E in lung
881 autopsies of 47 COVID-19 patients. PaO_2/FiO_2 (**B**) and A-a O_2 gradient (**C**) during
882 disease development of patients from Cluster 1 (N=16, green) and Cluster 2 (N=31,
883 red). *, $P < 0.05$ comparing the indicated groups, as determined by Area Under Curve
884 test. (**D-H**) Analysis of Cluster 1 and Cluster 2 for illness time (**D**), PaO_2/FiO_2 (**E**), A-a
885 O_2 gradient (**F**), fibrosis (**G**), and NLRP3 puncta per lung parenchyma area (**H**). Each
886 dot in the figure represents the value obtained from each individual. *, $P < 0.05$
887 comparing the indicated groups, as determined by Mann-Whitney test. (**I-J**)
888 Representative H&E images of lung parenchyma of 3 patients of cluster 1 (**I**) and 3
889 patients of cluster 2 (**J**). Scale bars 200 μm.

890

Supplementary Figures and Supplementary Figure Legends

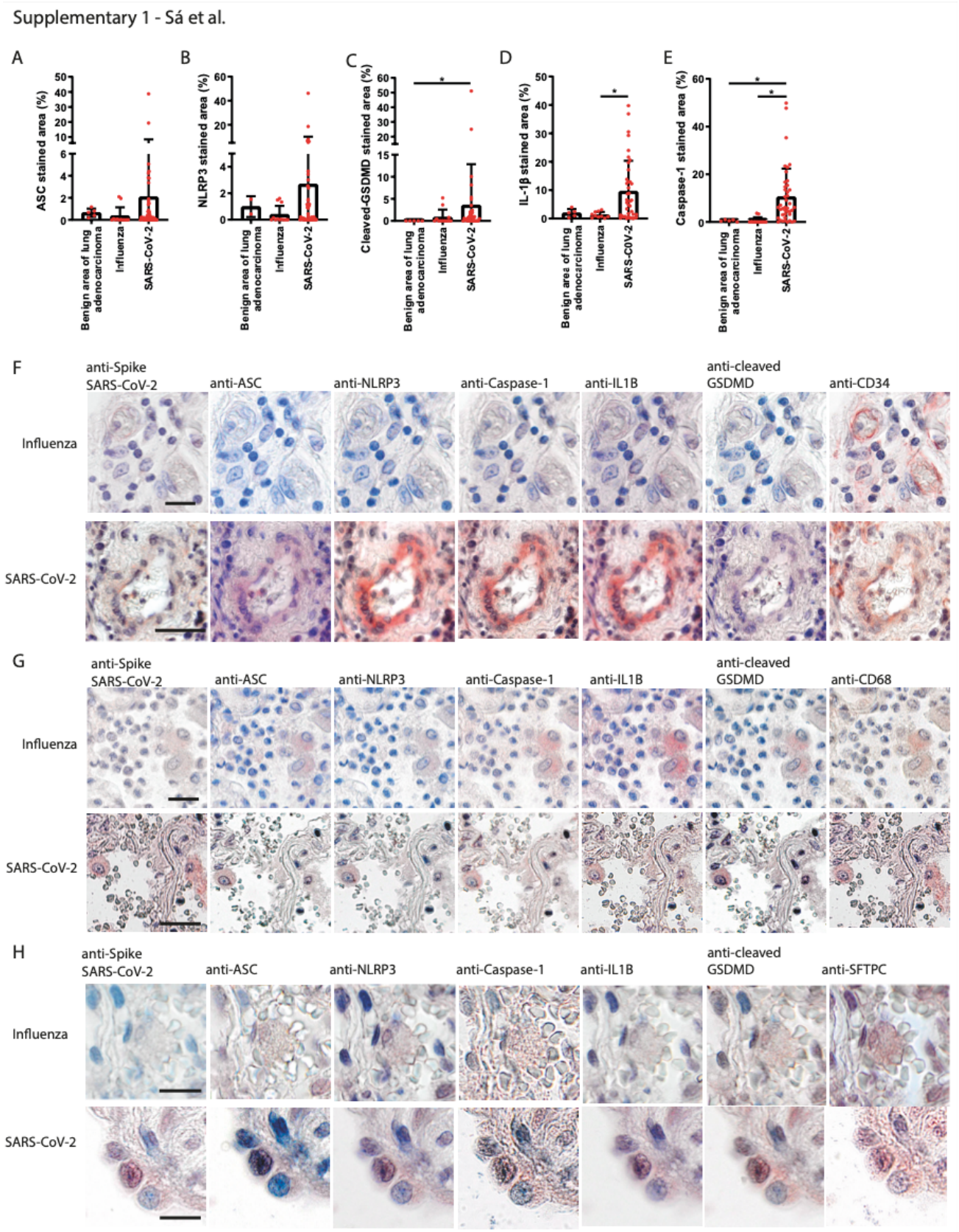

895

896

897 **Supplementary Fig. 1. Immunohistochemistry analysis of lung autopsies of**

898 **patients with COVID-19, influenza and lung adenocarcinoma.**

899 Immunohistochemistry analysis of lung autopsies of 47 COVID-19 patients, 12

900 influenza patients and 5 lung adenocarcinoma patients (benign area of the lungs).

901 Quantification of percentage of area stained for ASC (**A**), NLRP3 (**B**), cleaved GSDMD

902 (**C**), IL-1β (**D**) and Caspase-1 (**E**). (**F-H**) Representative images of lungs from fatal

903 cases of COVID-19 and Influenza, indicating colocalization of viral Spike, ASC,

904 NLRP3, Caspase-1, IL-1β and cleaved GSDMD in endothelial cells ($CD34^+$, **F**),

905 macrophages ($CD68^+$, **G**), and type II pneumocytes ($SFTPC^+$, **H**).

906

Supplementary 2 - Sá et al.

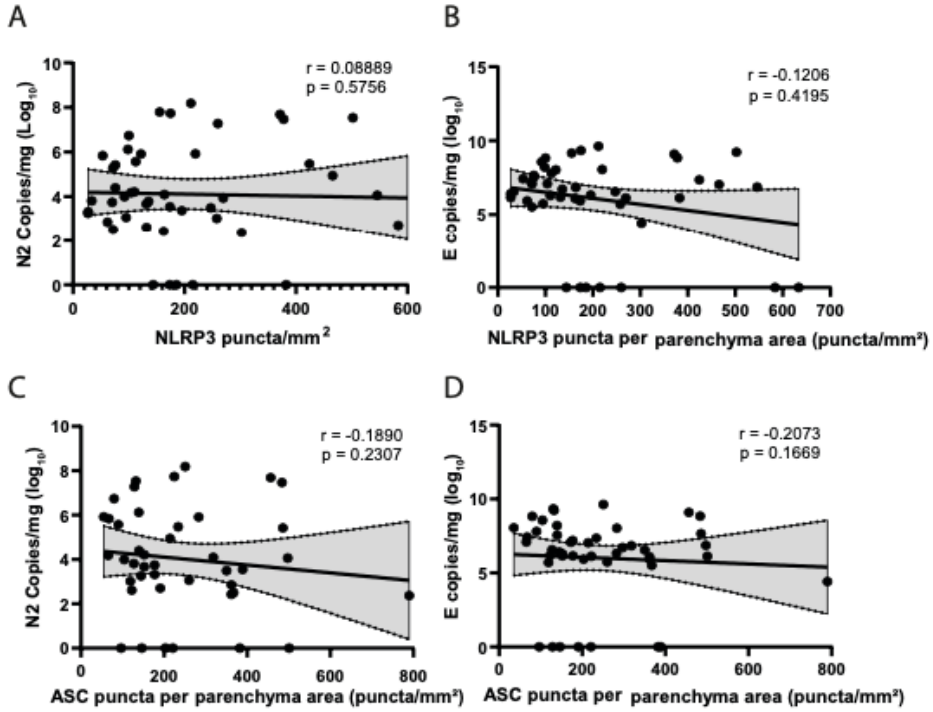

Supplementary Fig. 2. Non-significant correlation or viral loads and inflammasome activation in lethal cases of COVID-19 patients. Spearman correlation of pulmonary viral load and inflammasome activation in 47 fatal COVID-19 patients. (**A**) Correlation of viral N2 with NLRP3 puncta per parenchyma area; (**B**) Correlation of viral E with NLRP3 puncta per parenchyma area; (**C**) Correlation of viral N2 with ASC puncta per parenchyma area; (**D**) Correlation of viral E with ASC puncta per parenchyma area. r and p-value are indicated in the figure.

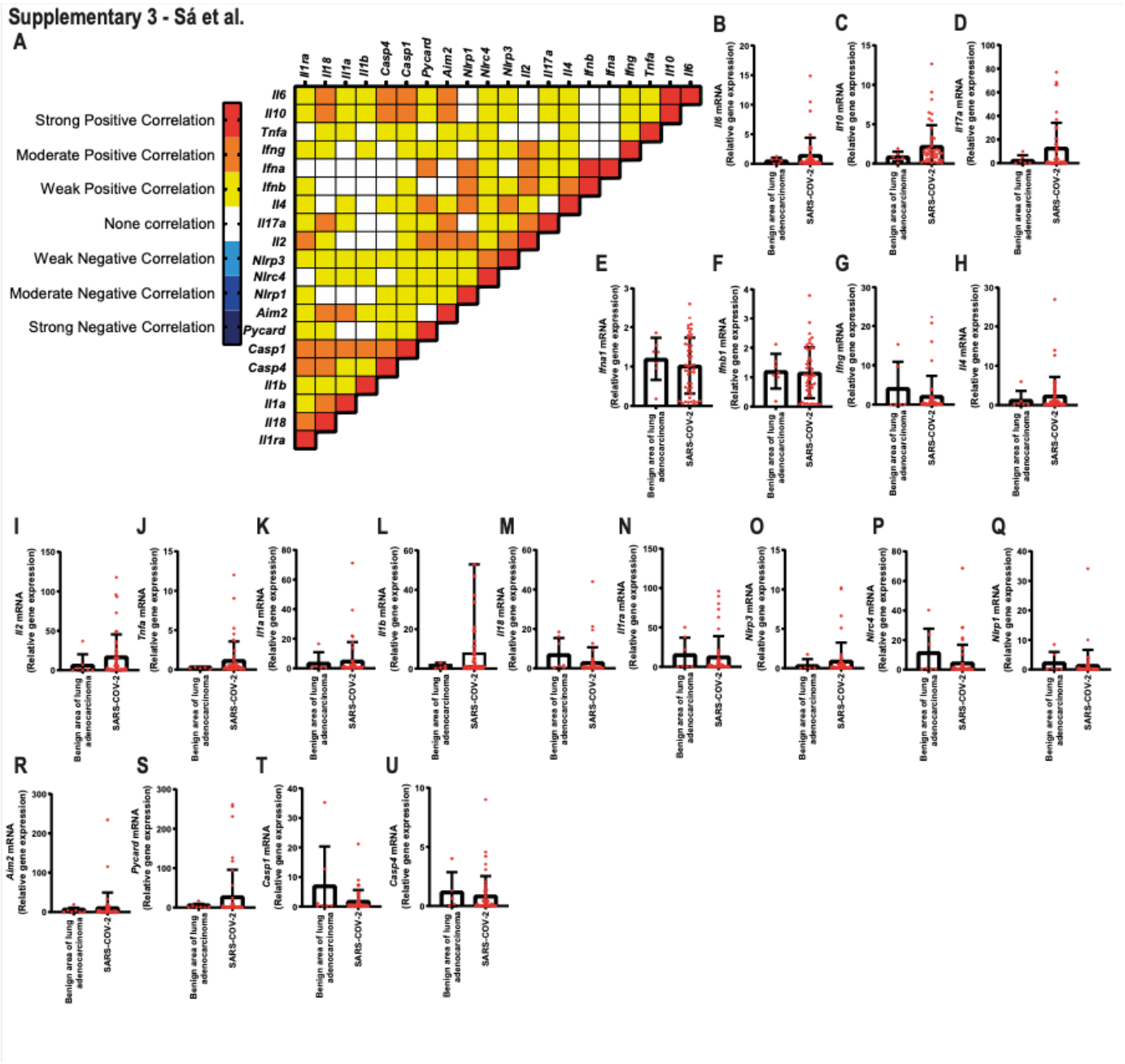
Supplementary 3 - Sá et al.
A
Strong Positive Correlation
Moderate Positive Correlation
Weak Positive Correlation
None correlation
Weak Negative Correlation
Moderate Negative Correlation
Strong Negative Correlation
Il1ra
Il18
Il1a
Il1b
Casp4
Casp1
Pycard
Aim2
Nlrp1
Nlrc4
Nlrp3
Il2
Il17a
Il4
Ifnb
Ifna
Ifng
Tnfa
Il10
Il6
B
Il6 mRNA (Relative gene expression)
C
Il10 mRNA (Relative gene expression)
D
Il17a mRNA (Relative gene expression)
E
Ifna1 mRNA (Relative gene expression)
F
Ifnb1 mRNA (Relative gene expression)
G
Ifng mRNA (Relative gene expression)
H
Il4 mRNA (Relative gene expression)
I
Il2 mRNA (Relative gene expression)
J
Tnfa mRNA (Relative gene expression)
K
Il1a mRNA (Relative gene expression)
L
Il1b mRNA (Relative gene expression)
M
Il18 mRNA (Relative gene expression)
N
Il1ra mRNA (Relative gene expression)
O
Nlrp3 mRNA (Relative gene expression)
P
Nlrc4 mRNA (Relative gene expression)
Q
Nlrp1 mRNA (Relative gene expression)
R
Aim2 mRNA (Relative gene expression)
S
Pycard mRNA (Relative gene expression)
T
Casp1 mRNA (Relative gene expression)
U
Casp4 mRNA (Relative gene expression)
Benign area of lung adenocarcinoma
SARS-COV-2

921

922

923 **Supplementary Fig. 3. Lung gene expression of COVID-19 patients.** Correlation
924 matrix of inflammasome and inflammatory gene expression in lung autopsy of 47
925 COVID-19 patients (**A**). Colors indicate correlation scores, categorized as positive
926 strong correlation (r ≥ 0.70; red); moderate positive correlation (0.50 ≥ r ≤ 0.70;
927 orange); weak positive correlation (0.30 ≥ r ≤ 0.50; yellow); negative strong correlation
928 (r ≥ -0.70; dark blue); negative moderate correlation (-0.50 ≥ r ≤ -0.70; blue) or
929 negative weak correlation (-0.30 ≥ r ≤ -0.50; light blue). Only correlations with $p<0.05$
930 are represented in the correlation matrix. (**B-U**) Expression of mRNA in the lung
931 autopsies of COVID-19 patients and lung adenocarcinoma patients (benign area of the
932 lungs). Selected genes were *Il6* (**B**), *Il10* (**C**), *Il17* (**D**), *Ifna1* (**E**), *Ifnb1* (**F**), *Ifng* (**G**), *Il4*
933 (**H**), *Il2* (**I**), *Tnfa* (**J**), *Il1a* (**K**), *Il1b* (**L**), *Il18* (**M**), *I1ra* (**N**), *Nlrp3* (**O**), *Nlrc4* (**P**), *Nlrp1* (**Q**),
934 *Aim2* (**R**), *Pycard* (**S**), *Casp1* (**T**), *Casp4* (**U**).

935

936

Supplementary 4 - Sá et al.

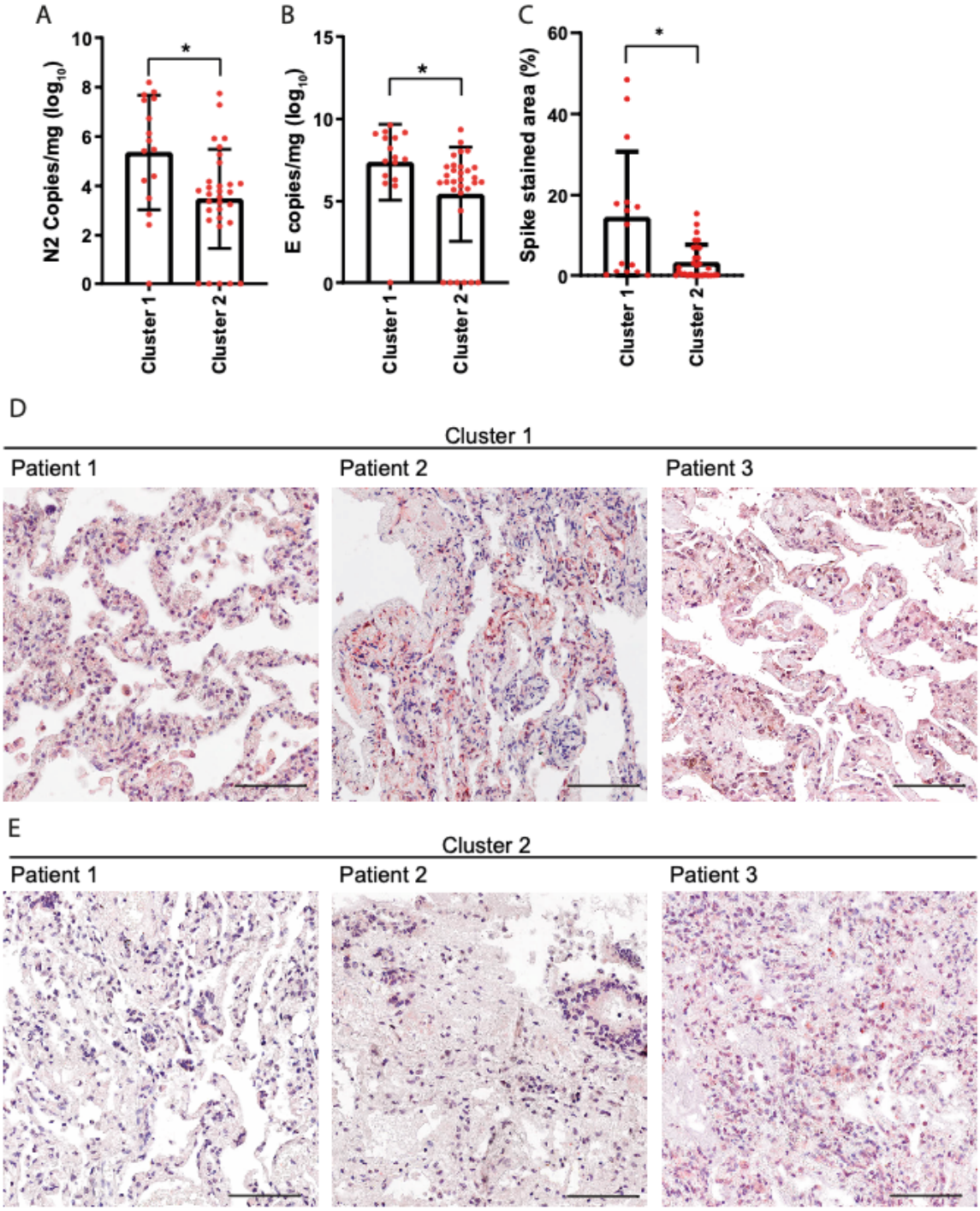

937

938

939

940

941 **Supplementary Fig. 4. COVID-19 patients from Cluster 1 contains higher viral**
942 **loads in the lungs as compared to patients from Cluster 2.** Quantification of viral
943 N2 (**A**) and E (**B**) in lung autopsies of 47 COVID-19 patients from Cluster 1 (N=16) and
944 Cluster 2 (N=31). (**C**) Quantification of percentage of area stained for viral Spike
945 protein in lung autopsies. Each dot in the figure represents the value obtained from
946 each individual. *, $P < 0.05$ comparing the indicated groups, as determined by Mann-
947 Whitney test. (**D-E**) Representative images of lungs tissues stained for Spike (red) and
948 Hematoxylin (blue). Scale bars 100 μm.

949

Supplementary 5 - Sá et al.

A

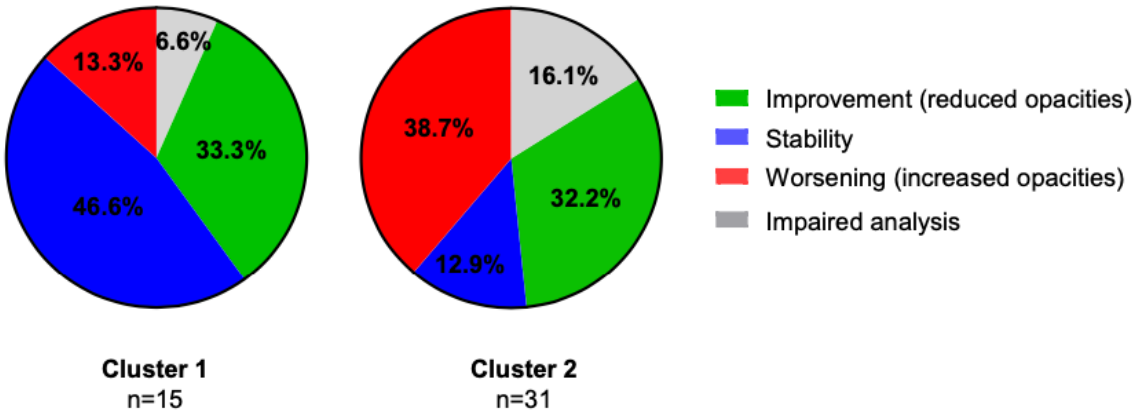

B

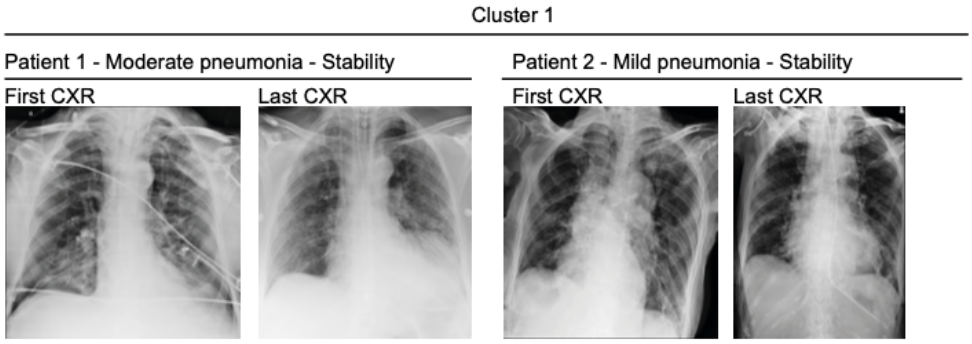

C

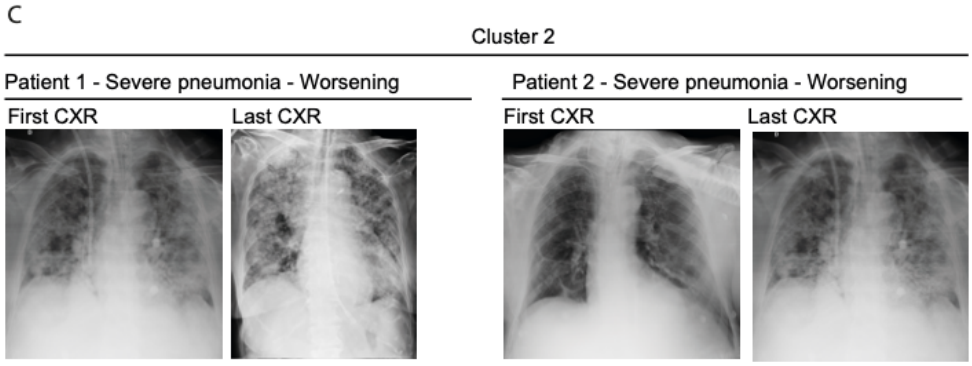

954

955

956 **Supplementary Fig. 5. CXR evolution of patients from Cluster 1 and Cluster 2.**

957 Analysis of the first and last Chest x-radiography (CXR) of 46 COVID-19 patients
958 belonging from Cluster 1 (n=15) and Cluster 2 (n=31). (**A**) patients with reduced
959 opacities (green), stability (blue) and increased opacities (red) comparing the fists and
960 first CXR. Impaired analyses are shown in gray. Representative images of first and
961 last CXR from two patients from Cluster 1, indicating stability in moderate and mild
962 pneumonia (**B**) and two patients from Cluster 2, indicating worsening conditions in
963 cases of severe pneumonia (**C**).

964

965

Supplementary Table 1. The list of primer sequences for real time-PCR

Gene	Sequence of primer (5'- 3')
Human *Nlrp3*	F: GGACTGAAGCACCTGTTGTGCA
	R: TCCTGAGTCTCCCAAGGCATTC
Human *Il1a*	F: TGTATGTGACTGCCCAAGATGAAG
	R: AGAGGAGGTTGGTCTCACTACC
Human *Il1ra*	F: ATGGAGGGAAGATGTGCCTGTC
	R: GTCCTGCTTTCTGTTCTCGCTC
Human *Nlrc4*	F: AGGTCCCACAACTCGTCAAGCT
	R: TGCTCACACGATTTCCCGCCAA
Human *Pycard*	F: AGCTCACCGCTAACGTGCTGC
	R: GCTTGGCTGCCGACTGAGGAG
Human *Nlrp1*	F: ATTGAGGGCAGGCAGCACAGAT
	R: CTCCTTCAGGTTTCTGGTGACC
Human *Casp1*	F: GCTGAGGTTGACATCACAGGCA
	R: TGCTGTCAGAGGTCTTGTGCTC
Human *Aim2*	F: GCTGCACCAAAAGTCTCTCCTC
	R: CTGCTTGCCTTCTTGGGTCTCA
Human *Il6*	F: AGACAGCCACTCACCTCTTCAG
	R: TTCTGCCAGTGCCTCTTTGCTG
Human *Gapdh*	F: GTCTCCTCTGACTTCAACAGCG
	R: ACCACCCTGTTGCTGTAGCCAA
Human *Tnf Alpha*	F: CTCTTCTGCCTGCTGCACTTTG
	R: ATGGGCTACAGGCTTGTCACTC
Human *Il10*	F: TCTCCGAGATGCCTTCAGCAGA
	R: TCAGACAAGGCTTGGCAACCCA
Human *Il1b*	F: CCACAGACCTTCCAGGAGAATG
	R: GTGCAGTTCAGTGATCGTACAGG
Human *Il18*	F: GATAGCCAGCCTAGAGGTATGG
	R: CCTTGATGTTATCAGGAGGATTCA
Human *Casp4*	F: GGGATGAAGGAGCTACTTGAGG
	R: CCAAGAATGTGCTGTCAGAGGAC
Human *Il17a*	F: CGGACTGTGATGGTCAACCTGA
	R: GCACTTTGCCTCCCAGATCACA
Human *Ifng*	F: GAGTGTGGAGACCATCAAGGAAG
	R: TGCTTTGCGTTGGACATTCAAGTC
Human *Ifnb1*	F: CTTGGATTCCTACAAAGAAGCAGC
	R: TCCTCCTTCTGGAACTGCTGCA
Human *Ifna1*	F: AGAAGGCTCCAGCCATCTCTGT
	R: TGCTGGTAGAGTTCGGTGCAGA
Human *Il4*	F: CCGTAACAGACATCTTTGCTGCC
	R: GAGTGTCCTTCTCATGGTGGCT